

**MINIATURIZATION OF WAVEGUIDE ANTENNAS USING
ELECTROMAGNETIC METAMATERIALS**

By

VIKRAM HEGDE

A THESIS

IN

ELECTRICAL ENGINEERING

Submitted to Graduate Faculty
of Texas Tech University in
Partial Fulfillment of
the requirement for
the Degree of

MASTER OF SCIENCE

IN

ELECTRICAL ENGINEERING

Approved

Mohammad A. Saed
Chairperson of the Committee

Thomas Trost

Accepted

Fred Hartmeister
Dean of the Graduate School

December, 2007

ACKNOWLEDGEMENTS

First and foremost, I would like to express my heartfelt gratitude towards my advisor, Dr. Mohammad Saed for providing me the opportunity, support and freedom to carry on this thesis. He was always extremely helpful in answering all my questions even by going out of the way. I am most grateful for his invaluable advice and saint-like patience to all my mistakes. His continuous financial support throughout my journey kept me afloat. I thank him from the bottom of my heart.

I wish to thank Dr. Thomas Trost for willing to be on my committee and for his never - ending interest, enthusiasm and ideas that showed me the right direction. All his valuable suggestions and inputs are highly appreciated. I am also thankful to him for due diligence in proofreading all of my manuscripts and this thesis.

It is my pleasure to acknowledge my peer roommates, Kushal Kapse, Amol Shelke and Raja Jayaraman for their friendship and company. I also thank my other friends who made my stay in Lubbock exciting and memorable.

I would like to thank all my colleagues, Rajnish, Faris, Spurthi, Avinash for all their hope and support.

Most importantly, what I am today is because of the love, support and faith showered by my family and friends back home in India. I am indebted to them and their presence is greatly missed.

TABLE OF CONTENTS

| | |
|--|-------------|
| ACKNOWLEDGEMENTS | <i>ii</i> |
| LIST OF FIGURES | <i>v</i> |
| ABSTRACT | <i>viii</i> |
| CHAPTER | |
| 1. INTRODUCTION | 1 |
| 1.1 Introduction | 1 |
| 1.2 Organization of the work | 2 |
| 2. ELECTROMAGNETIC METAMATERIALS | 4 |
| 2.1 Introduction | 4 |
| 2.2 Refractive Index | 5 |
| 2.3 Structure | 6 |
| 2.3.1 Negative Permittivity ($\epsilon < 0$) | 9 |
| 2.3.2 Negative Permeability ($\mu < 0$) | 11 |
| 2.4 Transmission Line Analysis of Left Handed materials | 15 |
| 3. WAVEGUIDE MINIATURIZATION USING ELECTROMAGNETIC METAMATERIALS | 24 |
| 3.1 Introduction | 24 |
| 3.2 Rectangular Waveguide | 25 |
| 3.3 Miniaturization | 26 |
| 4. THEORETICAL INVESTIGATIONS AND SIMULATIONS | 38 |
| 4.1 Introduction | 38 |
| 4.2 Ansoft HFSS TM FEM method | 38 |
| 4.3 Getting Started with HFSS | 40 |
| 4.4 Optimization | 42 |
| 4.5.1 Project Design | 43 |
| 4.5.2 HFSS model Setup | 48 |
| 4.5.3 Assigning excitation and boundary | 52 |
| 4.5.4 Solution setup and frequency sweep | 55 |
| 4.6 Solution and post processing | 58 |
| 4.7 Conclusion | 62 |

| | |
|---|----|
| 5. LABORATORY MEASUREMENTS | 63 |
| 5.1 Introduction | 63 |
| 5.2 Fabrication | 63 |
| 5.3 Experimental Setup and measurements | 65 |
| 6. CONCLUSIONS AND FUTURE DIRECTIONS | 73 |
| 6.1 Highlights | 73 |
| 6.2 Future work | 74 |
| REFERENCES | 76 |
| APPENDIX | |
| A. EQUIPMENT LIST | 82 |

LIST OF FIGURES

1.1: The geometry of the SRR-loaded square waveguide2

2.1: Classification of the materials based on constitutive parameters [44]6

2.2: Pendry’s (a) Thin Wire (TW) structure, negative ϵ /positive μ ($\vec{E} \parallel \vec{z}$) (b) Split Ring Resonators (SRR) structure, positive ϵ /negative μ ($\vec{H} \perp \vec{y}$) [11]7

2.3: First True “backward-wave media (BW media) Proposed by Smith *et al.* composed of Thin Wire (TW) and Split Ring Resonators (SRR). (a) 1D media. (b) 2D media. [10] ...8

2.4: Unit Cell of a periodic structure. Cell dimension a much smaller than the guided wavelength, λ_g ($a \ll \lambda_g$)8

2.5: Two dimensional subwavelength lattice of thin metal wire structure with a as unit cell dimension and r as radius of wire10

2.6: (a) Split Ring Resonator (SRR), (b) Two dimensional lattice of SRR structure with a as unit cell dimension12

2.7: Effective permeability of SRR’s [13]13

2.8: Equivalent circuit model of (a) Double SRR, (b) Single SRR [44]15

2.9: Equivalent circuit model of Brillouin and Pierce’s *backward wave* TL16

2.10: Lumped element equivalent circuit for purely RH lossy TL16

2.11: Lumped element equivalent circuit for purely RH lossless TL17

2.12: Lumped element equivalent circuit for purely LH lossless TL17

2.13: Lumped element equivalent circuit for CRLH TL18

2.14: ω - β dispersion-attenuation diagram for (a) Pure RH (b) Pure LH, and (c) CRLH TL from equation 2.23. [21]20

2.15: Equivalent circuit diagram of balanced CRLH21

2.16: ω - β , dispersion-attenuation diagram of balanced CRLH22

2.17: Refractive index of balanced (blue) and unbalanced (red) CRLH23

3.1: Rectangular waveguide25

3.2: The split ring resonator (SRR) geometry used in [7] $r = 1.4$ mm, $c = 0.5$ mm, $d = 0.2$ mm, $t = 0.49$ mm, $\epsilon = 2.43\epsilon_0$ 27

3.3: The split ring resonator (SRR) loaded square cross section waveguide ($a = 6$ mm) [7]27

3.4: Experimental setup used in [7] ($l = 36$ mm)28

3.5: Transmission coefficient (S_{12}) as reported in [7] ($l = 36$ mm)28

3.6: Capacitively loaded loop antenna and equivalent circuit diagram [29]29

| | |
|---|----|
| 3.7: Square waveguide filled with SRR [8] | 31 |
| 3.8: Effect of filling material in the waveguide | 33 |
| 3.9: Transmission line representation of a rectangular waveguide [8] | 34 |
| 3.10: Inductance and capacitance model of figure 3.7 [8] | 34 |
| 3.11: Equivalent circuit of a waveguide filled with uniaxial material [8] | 35 |
| 3.12: Broadside coupled SRR | 37 |
| 4.1: HFSS Desktop with interactive menu and tool bars | 41 |
| 4.2: Different structures tried for antenna miniaturization | 42 |
| 4.3: HFSS model of the setup | 44 |
| 4.4 (a): Return loss for 9 rings placed in a waveguide of 60 mm long | 45 |
| 4.4 (b): Return loss for 10 rings placed in a waveguide of 60 mm long (flush) | 45 |
| 4.4 (c): Return loss for 11 rings placed in a waveguide of 60 mm long | 46 |
| 4.4 (d): Return loss for 13 rings placed in a waveguide of 60 mm long | 46 |
| 4.5: HFSS model of waveguide antenna with 13 E-SRR placed in symmetry plane | 47 |
| 4.6: Return loss for the E-SRR loaded waveguide antenna | 48 |
| 4.7: HFSS project manager | 49 |
| 4.8: Selecting unit of measurement for drawing | 49 |
| 4.9: Property window | 50 |
| 4.10: Unit cell | 51 |
| 4.11: Duplicate along axis command | 51 |
| 4.12: Array of twelve BC-SRRs | 52 |
| 4.13: Wave port assignment | 53 |
| 4.14: Boundary Assignment | 54 |
| 4.15: Boundary and excitations in project manager window | 55 |
| 4.16: Solution Setup | 56 |
| 4.17: Frequency Sweep | 57 |
| 4.18: Validation Check | 58 |
| 4.19: Plot selection | 58 |
| 4.20: Return loss for the BC-SRR loaded waveguide antenna | 59 |
| 4.21: Phase (dotted) and magnitude (solid) of S_{11} for BC-SRR loaded waveguide antenna | 60 |
| 4.22: E plane radiation pattern for BC-SRR loaded waveguide antenna (solid – co polarized, dotted – cross polarized) | 61 |

| | |
|---|----|
| 4.23: H plane radiation pattern for BC-SRR loaded waveguide antenna (solid – co polarized, dotted – cross polarized) | 61 |
| 5.1: Photograph of Array of twelve BC-SRR | 64 |
| 5.2: Unit cell dimensions | 64 |
| 5.3: Schematic of the prototype antenna | 65 |
| 5.4: Photograph of the prototype antenna | 66 |
| 5.5: Measured return loss of the antenna | 66 |
| 5.6: Screen shot of network analyzer | 67 |
| 5.7: Measured phase of input return loss (S_{11}) | 68 |
| 5.8: Measured and simulated return loss of the antenna | 69 |
| 5.9: Experimental setup for measurement of radiation pattern | 69 |
| 5.10: Measured E plane co- and cross polarized radiation pattern | 70 |
| 5.11: Measured H plane radiation pattern | 71 |
| 5.12: Comparison of measured and computed E plane radiation pattern | 72 |

ABSTRACT

In the era of miniaturized hand - held devices rectangular waveguides have been replaced by planar guiding structures in many of the applications for miniaturizations. Use of waveguides is inevitable in many applications. Waveguides offer a number of advantages over planar guiding structures, viz., lower loss and high power handling capability, absence of substrate mode losses etc. Waveguide manufacturing cost and their size at microwave frequencies are the biggest disadvantages. Over the years a number of researchers have tried to miniaturize waveguides. Classical waveguide miniaturization is by filling the waveguides with a dielectric yielding to size reduction of $1/\sqrt{\epsilon_r}$ relative to an empty waveguide. The disadvantages of such dielectric filled waveguides are, high cost and such waveguides cannot be used as an antenna.

In this thesis we propose an open - ended rectangular waveguide antenna loaded with broadside coupled split - ring resonators (BC-SRR) radiating below the cutoff frequency of the waveguide. An X-Band, open - ended waveguide antenna loaded with BC-SRR operating in a 5.5-6.7 GHz frequency band was designed, fabricated and tested.

CHAPTER 1

INTRODUCTION

1.1 Introduction

Although planar guiding structures have replaced rectangular waveguides in many of applications for miniaturizations, waveguides are still needed in many applications. Waveguides offers the advantages of lower loss and high power handling capability. Planar antennas such as patch antennas have disadvantages such as substrate mode losses, spurious radiation from feeding networks, and poor polarization purity. However, owing to the three dimensional nature of waveguide antennas, they can be difficult to integrate with planar circuitry and are excessively large at low frequencies.

It is known from electromagnetics that for propagation of waves through a waveguide, the width of the waveguide cross section must be at least one half of the wavelength [1]. Classical waveguide miniaturization was done by filling the waveguides with a dielectric material [2]-[5]. Their size, relative to empty waveguide, is reduced by a factor of $1/\sqrt{\epsilon_r}$, where ϵ_r is the dielectric constant. However, air-filled waveguides have a lower loss than the equivalent dielectric filled waveguide. Furthermore, high ϵ_r dielectric - filled waveguides do not radiate from the open end as effectively as air filled waveguides.

In the last few years, there have been several new ideas which may lead to the miniaturization of waveguides. Artificial perfect magnetic conductors (complex surfaces) were used for waveguide walls in [6] providing TEM propagation. This phenomenon could be used for reduction of the waveguide width. Recently, a very unusual waveguide was proposed by Marques *et al.* in [7] and then extensively studied by Hrbar *et al.* in [8]. Marques *et al.* proposed a rectangular metallic waveguide periodically loaded with resonant magnetic scatterers, so-called split - ring resonators (SRR's) [8]-[10], [30], [41], [42]. The geometry of the Marques waveguide is presented in Figure 1.1. The SRR's in the waveguide are oriented so that their magnetic moments are orthogonal to the

waveguide axis and to one of the walls. The waveguide supports a propagating mode within a frequency band near the resonance of SRR's even if it is located below the cutoff frequency of the hollow waveguide [7], [8]. For operation below cutoff, the transverse dimensions of the waveguides are much smaller than the wavelength in free space. Thus, loading by SRR's provides a unique method for the miniaturization of guiding structures.

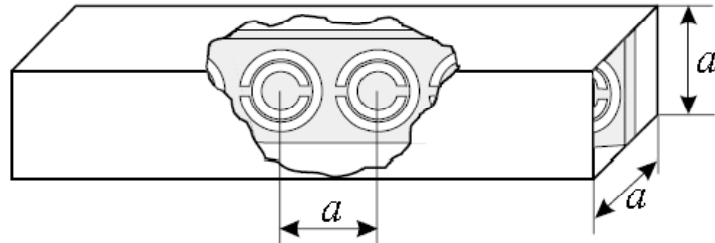


Figure 1.1: The geometry of the SRR-loaded square waveguide.

SRR's belong to a broader class of materials called electromagnetic metamaterials. Metamaterials are defined as macroscopic composites having a man-made, three dimensional, periodic cellular architecture designed to produce an optimized combination, not available in nature, of two or more responses to a specific excitation. Each cell contains metaparticles, macroscopic constituents designed with low dimensionality that allow each component of the excitation to be isolated and separately maximized. In this thesis, SRR's are used for miniaturizing a waveguide antenna by loading single array SRR's in the symmetry plane of the waveguide.

1.2 Organization of the work

Following this brief introduction, Chapter 2 introduces the reader to basic electromagnetic metamaterials, different structures, and special properties with a brief history of material evolution. The chapter also presents a brief recapitulation of previous work in miniaturization of waveguides using metamaterials. Chapter 3 introduces a novel method of waveguide miniaturization using electromagnetic metamaterials capable of

supporting backward waves. Chapter 4 focuses on a simulation set up of proposed miniaturized electromagnetic metamaterial - loaded waveguide antenna, with Ansoft HFSS, a full wave finite element electromagnetic solver. Chapter 4 also presents various simulation results. Chapter 5 compares the above proposed new design simulation with experimental results. Chapter 6 presents conclusions and some recommendations for future work.

CHAPTER 2

ELECTROMAGNETIC METAMATERIALS

2.1 Introduction

The electromagnetic properties of a material can be described by its permittivity and permeability. These two parameters macroscopically describe the effects of induced electric and magnetic polarization.

In 1967, Russian physicist Viktor Veselago theoretically analyzed plane wave propagation in a substance with simultaneous negative ϵ and μ [45]. His study proposed that in such substances, direction of the Poynting vector is antiparallel to the direction of phase velocity. For this reason, Veselago referred such media as “left handed media”. For such media with negative permittivity and permeability, many names have been suggested such as “electromagnetic metamaterials” [8]-[10], [19], [25], “backward-wave media (BW media)” [46]-[47], “Double-negative (DNG) metamaterials” [48]-[49], to name a few. Metamaterials have opened an exciting field to realize unexpected physical properties and applications, which are not possible from naturally occurring materials. Conductive or dielectric inclusions in metamaterials can be tailored in shape and size, periodicity, and defects to produce unusual yet exciting properties. Unusual properties such as, negative permittivity and permeability, negative refraction at the interface of two (RH and LH) media, reversal of Snell’s law, reverse Doppler effect, and amplification of evanescent waves can be realized. However, since such materials are not readily available in nature, Veselago’s predictions did not become popular in research community until Smith et al. in [30] succeeded in constructing a material using split - ring resonators (SRR’s) and straight conducting wires which yielded negative values of ϵ and μ and thus a negative index of refraction over a finite band of frequencies in the microwave region. In 2003, Science magazine named left-handed electromagnetic metamaterials as one of the top ten scientific breakthroughs of 2003.

2.2 Refractive Index

Propagation of EM waves with in a medium can be described by two parameters, namely, permittivity, ϵ , and permeability μ , (constitutive parameters). Permittivity ϵ describes the relation between electric field strength \vec{E} and electric displacement \vec{D} . Permeability μ describes the relation between magnetic field strength \vec{H} and magnetic flux density \vec{B} . For an isotropic material, the dispersion equation is given by:

$$k^2 = \frac{\omega^2}{c^2} n^2 \quad (2.1)$$

In the above equation refractive index, n is given by:

$$n = \pm \sqrt{\frac{\epsilon\mu}{\epsilon_0\mu_0}} = \pm \sqrt{\epsilon_r\mu_r} \quad (2.2)$$

where ϵ_r and μ_r are the relative permittivity and permeability related to the free space permittivity and permeability, $\epsilon_0 = 8.854 \times 10^{-12} F/m$ and $\mu_0 = 4\pi \times 10^{-7} H/m$ respectively. From equation 2.2, it can be noted that there are four possible sign combinations for ϵ_r and μ_r . A medium with positive permittivity and permeability ($\epsilon_r > 0$, $\mu_r > 0$), which constitutes most naturally occurring media (e.g., dielectrics) is called a double positive (DPS) medium. A medium with negative permittivity and positive permeability ($\epsilon_r < 0$, $\mu_r > 0$), such as some plasmas (e.g., metals at optical frequency) is called an epsilon-negative (ENG) medium. A medium with positive permittivity and negative permeability ($\epsilon_r > 0$, $\mu_r < 0$), (e.g., ferrimagnetic materials) is called mu-negative (MNG) medium. Finally, medium with simultaneously negative permittivity and negative permeability ($\epsilon_r < 0$, $\mu_r < 0$) is called a double negative medium (DNG) or left-handed (LH) material. The graphical representation of the above properties is shown in figure 2.1.

The interesting point is that for simultaneously negative values of ϵ_r and μ_r , a left-handed vector triplet of E, H and k is formed. The refractive index is negative;

$$n = -\sqrt{\epsilon_r\mu_r} \quad (2.3)$$

However, the intrinsic impedance of the medium still remains positive.

$$Z = \sqrt{\frac{\mu_r}{\epsilon_r}} \quad (2.4)$$

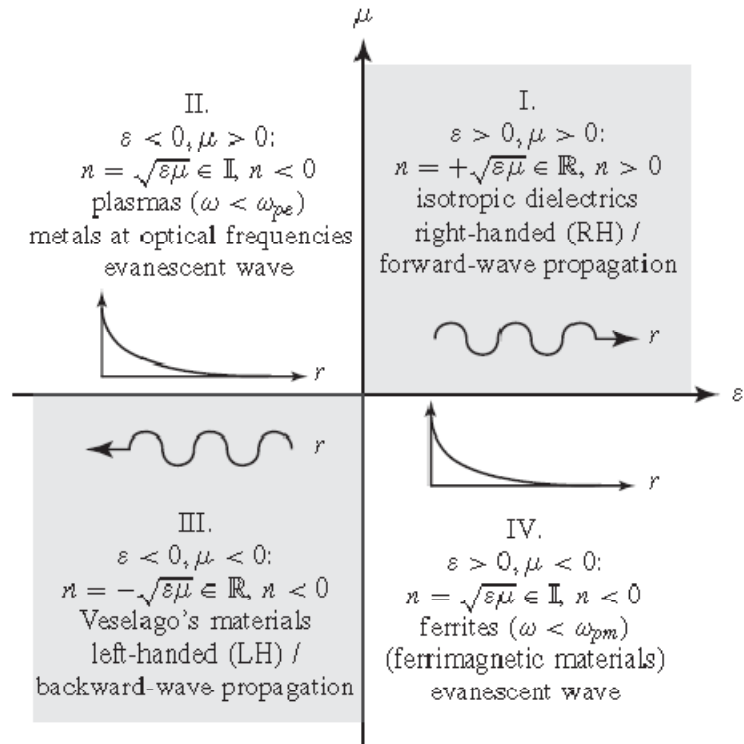


Figure 2.1: Classification of the materials based on constitutive parameters [44].

2.3 Structure

The idea of metamaterials began with Veselago's paper in 1967, who proposed EM wave propagation in hypothetical material with simultaneous negative permittivity ϵ and negative permeability μ . Though materials with one of the constitutive parameters negative were known (ϵ negative, metals at optical frequency; μ negative, ferrimagnetic materials), which support no wave propagation (waves are evanescent), a true LH

material was not a natural substance, as expected by Veselago. Veselago's findings did not come to main stage research until 30 years later when, in 1996, Pendry [11] at Imperial College, London, suggested the plasmonic type negative ϵ , positive μ and positive ϵ , negative μ periodic structures in microwave frequency range. The structures consisted of array of conducting Thin Wires (TW) at suitably chosen spacing and diameter which would have negative permittivity in designed frequency range. Three years later, Pendry proposed a different type of array, composed of conducting split - ring resonators (SRR) that could have negative permeability over certain range of frequencies. Pendry's structures are shown in the figure 2.2.

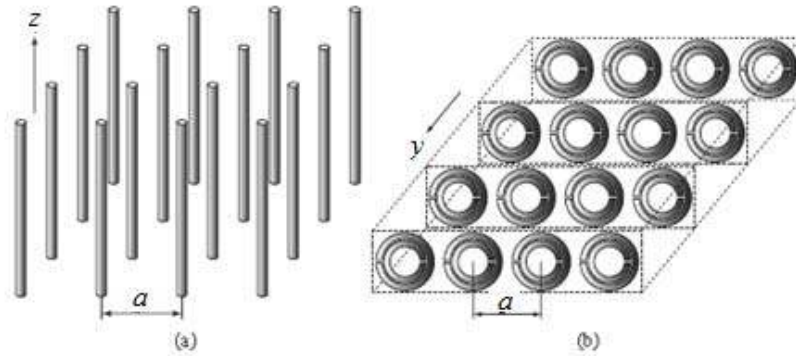


Figure 2.2: Pendry's (a) Thin Wire (TW) structure, negative ϵ /positive μ ($\vec{E} \parallel \vec{z}$) (b) Split - Ring Resonators (SRR) structure, positive ϵ /negative μ ($\vec{H} \perp \vec{y}$) [11]

Inspired by Pendry's work, Smith *et al.*[30] from University of California, San Diego (UCSD), proposed an artificial effectively homogeneous metamaterial structure with simultaneous negative permittivity ϵ and negative permeability μ . The structure essentially was a composite of two of the Pendry's structures (TW and SRR) as shown in figure 2.3.

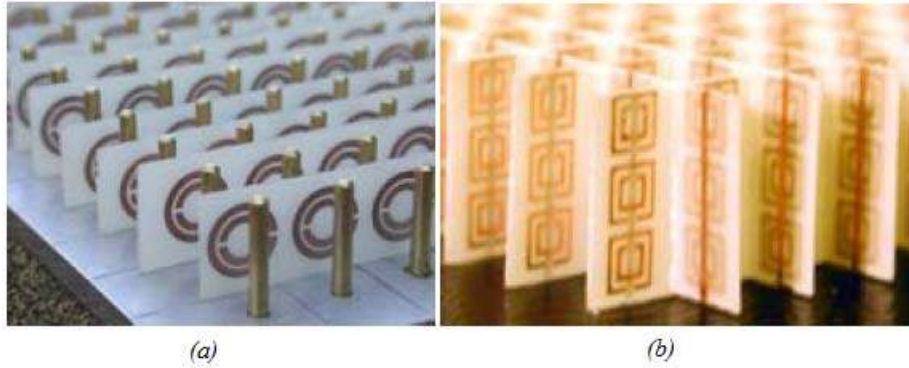


Figure 2.3: First True “backward-wave media (BW media) Proposed by Smith *et al.* composed of Thin Wire (TW) and Split - Ring Resonators (SRR). (a) 1D media. (b) 2D media. [10].

Both of these metamaterial structures (Pendry and Smith, *et al.*) aimed to engineer unit cells with an average cell size a (figure 2.4) much smaller than the guided wavelength λ_g ($a \ll \lambda_g$) and to integrate them into a bulk, homogeneous material while still preserving their material properties.

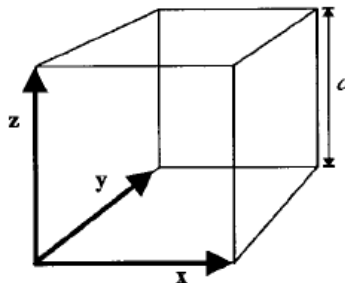


Figure 2.4: Unit Cell of a periodic structure. Cell dimension a much smaller than the guided wavelength, λ_g ($a \ll \lambda_g$).

Over the years, many different structures have been proposed to engineer negative ϵ and negative μ at different frequencies ranging from a few MHz to THz.

2.3.1 Negative Permittivity ($\epsilon < 0$)

A structure consisting of very thin metal wires arranged in a three-dimensional cubic lattice can model the response of dilute plasma. The plasmon is a well established collective excitation of metals i.e. a collective oscillation of electron density [11]-[12]. In equilibrium the charge on the electron gas is compensated by the background nuclear charge. On disturbing the neutrality, a surplus of uncompensated charge is generated at the ends of the specimen, with opposite signs at the opposite ends supplying a restoring force resulting in a simple harmonic motion with plasma frequency ω_p ,

$$\omega_p^2 = \frac{ne^2}{\epsilon_0 m_{eff}} \quad (2.5)$$

where, n is the electron density, m_{eff} is the electron mass and e is the electron charge.

For a two - dimensional subwavelength lattice of thin metal wire structure (figure 2.5) subjected to EM radiation with electric field parallel to the wires, the collective EM response of the material is characterized by a lower effective plasma frequency given by,

$$\omega_p^2 = \frac{2\pi c_0^2}{a^2 \ln\left(\frac{a}{r}\right)} \quad (2.6)$$

where, c_0 is the velocity of light in vacuum, a is the lattice constant of the wire array, and r is the radius of the cylindrical wire.

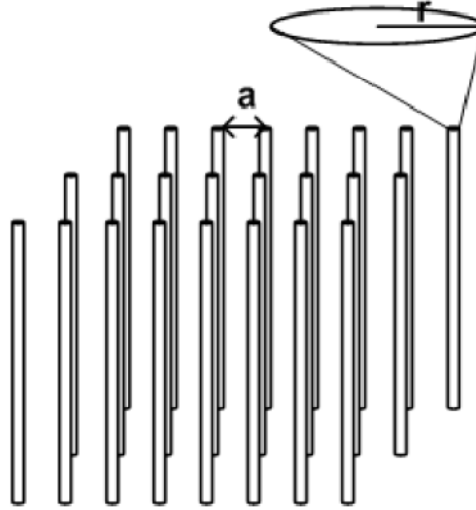


Figure 2.5: Two dimensional subwavelength lattice of thin metal wire structure with a as unit cell dimension and r as radius of wire.

The metallic wires cell size a (figure 2.5) is much smaller than the guided wavelength λ_g ($a \ll \lambda_g$). When the wavelength of the incident radiation is much larger than the cell size of a collection of scatterers, the response of the scatterers to the incident fields can be treated by way of the effective medium theory.

In the thin wire case, the effective medium theory holds since corresponding λ_g for ω_p is much larger than the radius of the wires. Therefore, an effective dielectric permittivity, ϵ_{eff} , can be used to define the permittivity of the medium. As far as external electromagnetic radiation is concerned, a thin wire structure appears as an effectively homogeneous dielectric medium whose internal structure is only apparent as it dictates ϵ_{eff} [11]. ϵ_{eff} is given by,

$$\epsilon_{eff} = 1 - \frac{\omega_p^2}{\omega(\omega + \frac{i\epsilon_0 a^2}{\pi r^2 \sigma})} \quad (2.7)$$

where σ is the conductivity of metal.

Let

$$\gamma = \frac{\epsilon_0 a^2}{\pi r^2 \sigma} \quad (2.8)$$

where, γ is the damping factor due to metal losses.

Substituting (2.8) in (2.7),

$$\epsilon_{eff} = 1 - \frac{\omega_p^2}{\omega^2 + \gamma^2} + i \frac{\gamma \omega_p^2}{\omega(\omega^2 + \gamma^2)} \quad (2.9)$$

The significance of the above equation is that at frequencies just below the plasma frequency the permittivity is negative with relatively low damping and the index of refraction becomes imaginary.

2.3.2 Negative Permeability ($\mu < 0$)

Electric response of a dielectric is governed by its electric charge, which also determines its permittivity. It is very difficult to have a material with negative permeability, because there is nothing analogous to electric charge in the magnetic domain. All naturally occurring materials have positive magnetic permeability. In 1999, Pendry et al. [13] proposed several microstructured metallic conducting scattering elements displaying a magnetic response to an applied electromagnetic field when grouped into an interacting periodic array. These structures consisted of loops of conductors with a gap. These structures were much smaller than the guided wavelength, λ_g ($a \ll \lambda_g$). These structures were resonant due to the internal capacitance and inductance and were called split - ring resonators (SRR). Figure 2.6 shows the Pendry *et al.* SRR structure.

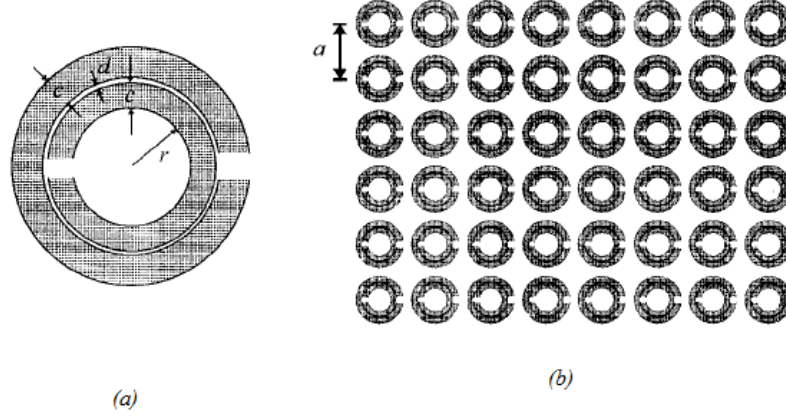


Figure 2.6: (a) Split - Ring Resonator (SRR), (b) Two dimensional lattice of SRR structure with a as unit cell dimension.

A single SRR can be thought of as a small, capacitively loaded loop antenna. If this antenna is slightly above resonant frequency, the local scattered magnetic field will be out of phase with the incident field. This will result in a local magnetic field lower than the incident field. This will give rise to a negative magnetic polarization and effective negative permeability for the material. Since the structure is smaller than the incident wavelength, the following equation holds for such a medium [13],

$$\begin{aligned} B_{ave} &= \mu_{eff} \mu_0 H_{ave} \\ D_{ave} &= \epsilon_{eff} \epsilon_0 H_{ave} \end{aligned} \quad (2.10)$$

Also, [13] proposes, for a SRR medium,

$$\mu_{eff} = 1 - \frac{F}{1 + \frac{2i\sigma}{\omega r \mu_0} - \frac{3}{\pi^2 \mu_0 \omega^2 C r^3}} \quad (2.11)$$

where F is the fractional volume occupied by the interior of the unit cell, and r is the radius of the inner ring. Fractional F is given by,

$$F = \frac{\pi r^2}{a^2} \quad (2.12)$$

where a is the lattice constant. C is the capacitance per unit area between the sheets and given by,

$$C = \frac{\epsilon_0}{d} = \frac{1}{dc_0^2 \mu_0} \quad (2.13)$$

where d is the distance between the two rings. Substituting equations 2.12 and 2.13 in equation 2.11;

$$\mu_{eff} = 1 - \frac{\frac{\pi r^2}{a}}{1 + \frac{2i\sigma}{\omega r \mu_0} - \frac{3dc_0^2}{\pi^2 \mu_0 \omega^2 r^3}} \quad (2.14)$$

Since we now have capacitance in the system that can balance the inductance present, μ_{eff} becomes resonant, which is shown in figure 2.7.

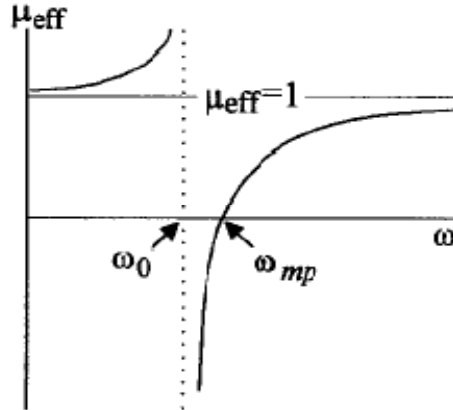


Figure 2.7: Effective permeability of SRR's [13].

ω_0 is the frequency at which μ_{eff} diverges,

$$\omega_0 = \sqrt{\frac{3}{\pi^2 \mu_0 C r^3}} = \sqrt{\frac{3dc_0^2}{\pi^2 r^3}} \quad (2.15)$$

ω_{mp} is the magnetic plasma frequency,

$$\omega_{mp} = \sqrt{\frac{3}{\pi^2 \mu_0 C r^3 (1-F)}} = \sqrt{\frac{3dc_0^2}{\pi^2 r^3 (1-\frac{\pi r^2}{a^2})}} \quad (2.16)$$

Above analysis [13] shows that the effective permeability of the medium is;

$$\mu_{eff} = 1 - \frac{F\omega^2}{\omega^2 - \omega_0^2 + i\gamma\omega} \quad (2.14)$$

The above equation shows that propagation occurs up to the frequency ω_0 , followed by a band gap where there is no propagation, followed by propagation starting at frequency ω_{mp} . The reason for the gap in propagation is of particular significance, since effective permeability will become negative for this frequency region. Referring to Figure 2.7, the real part of the permeability increases from unity at $\omega = 0$ to a large positive values near $\omega = \omega_0$, where it then abruptly passes to a large negative value, crossing $\mu = 0$ at $\omega = \omega_{mp}$. The peak value of the permeability is constrained by the magnitude of the material loss in the SRR. The width of the negative permeability region is determined by the filling factor F as in Equation 2.12. At high frequencies the permeability tends toward $\mu_{eff} = 1$, however, it is understood that the material will stop responding at a very high frequency, and the permeability will reach to unity.

Figure 2.8 shows the equivalent circuit diagram of SRR's [44]. A single ring in the unit cell produces identical effects. But the presence of a second ring increases the overall current path and mutual capacitance. This increases magnetic activity, bandwidth, and effective permeability.

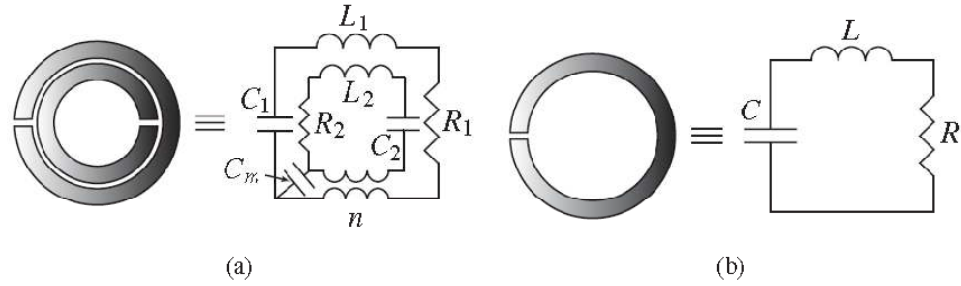


Figure 2.8: Equivalent circuit model of (a) Double SRR, (b) Single SRR [44].

In the double ring configuration, capacitive coupling and inductive coupling between the two rings are modeled by a coupling capacitance C_m and by a transforming ratio n . In the single ring configuration, the circuit model is that of the simplest RLC resonator with

resonant frequency $\omega_0 = \frac{1}{\sqrt{LC}}$.

2.4 Transmission Line Analysis of Left Handed materials

Transmission line theory has been a powerful tool for analysis and design on conventional electromagnetic waveguiding structures. Long before Viktor Veselago, in late 1940s', the term *backward waves* [14, 15] was used by Brillouin and Pierce. They demonstrated wave propagation with negative phase and group velocity. Periodic structure used by Brillouin had negative space harmonics in Fourier series expansion of fields [14]. Pierce *et al.* demonstrated backward wave amplification in Travelling Wave Tubes [15]. Setups used both by Brillouin and Pierce had an equivalent circuit model with series capacitance and shunt inductance as shown in figure 2.9 forming a backward wave transmission line (TL) similar to a lumped delay line.

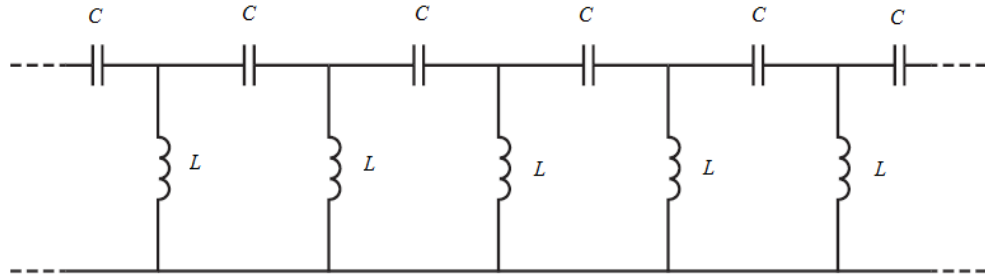


Figure 2.9: Equivalent circuit model of Brillouin and Pierce's *backward wave* TL.

Conventional backward wave models including Brillouin's and Pierce's structures typically had a unit cell size of the order of half or multiple of half the guided wavelength ($p \approx \lambda_g/2$ or $p \approx n\lambda_g/2$). Such structures supported backward waves associated with space harmonics or higher order modes due to diffraction and scattering phenomenon which are not related to constitutive parameters (ϵ_r and μ_r) and refractive index (n). Such structures, which cannot be characterized by their constitutive parameters, would not exhibit electromagnetic properties of real materials (Dielectrics like Teflon, Duroid, Glass).

Based on Brillouin and Pierce's equivalent circuit model, in 2002 several research groups, viz. Caloz *et al.* [16, 17] and Eleftheriades *et al.* [18, 19], proposed a similar Transmission Line (TL) approach for electromagnetic metamaterials.

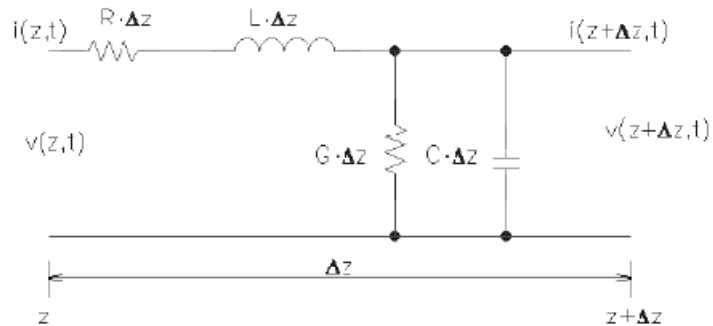


Figure 2.10: Lumped element equivalent circuit for purely RH lossy TL.

Figure 2.10 shows homogeneous model of purely right handed (RH) circuit for an incremental length of lossy transmission line (TL). For simplicity, only lossless line will be considered, as shown in figure 2.11.

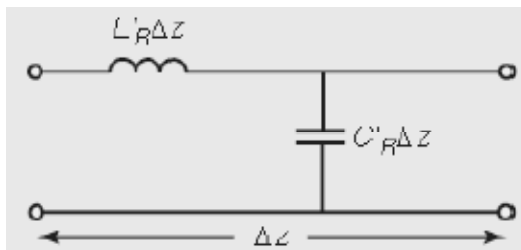


Figure 2.11: Lumped element equivalent circuit for purely RH lossless TL.

The dual of figure 2.11, a pure RH TL, is a left-handed transmission line (LH TL) with series capacitance and shunt inductance is shown in figure 2.12. Subscripts R and L are used to denote left or right-handedness of the lines.

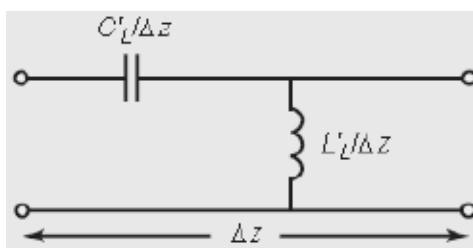


Figure 2.12: Lumped element equivalent circuit for purely LH lossless TL.

The complex propagation constant for the above circuit is given by;

$$\gamma = j\beta = \frac{1}{j\omega\sqrt{L'_L C'_L}} = -j \frac{1}{j\omega\sqrt{L'_L C'_L}} \quad (2.15)$$

$$\beta = -\frac{1}{\omega\sqrt{L'_L C'_L}} \quad (2.16)$$

From equation 2.16, it can be seen that propagation is backwards. The phase velocity and group velocities are given by;

$$v_p = \frac{\omega}{\beta} = -\omega^2 \sqrt{L'_L C'_L} \quad (2.17)$$

$$v_g = \left(\frac{d\beta}{d\omega} \right)^{-1} = \omega^2 \sqrt{L'_L C'_L} \quad (2.18)$$

Equation 2.17 and equation 2.18, show that the phase velocity and group velocity in LHTL are antiparallel. The phase velocity v_p denotes direction of phase of propagation. The group velocity v_g denotes direction of power flow (Poynting vector). The characteristic impedance of the transmission line is given by;

$$Z_0 = \sqrt{\frac{Z'}{Y'}} = \sqrt{\frac{L'_L}{C'_L}} \quad (2.19)$$

Equations 2.15 through equation 2.19 show that the transmission line in figure 2.10 is purely left handed (LH TL).

The presence of parasitics (series inductance due to current flow in metallization and shunt capacitance due to voltage gradient) makes pure LH TL non realizable. More realistic Composite Right/Left Handed (CRLH) (introduced in [20] by Caloz *et al.*) transmission line is shown in figure 2.13.

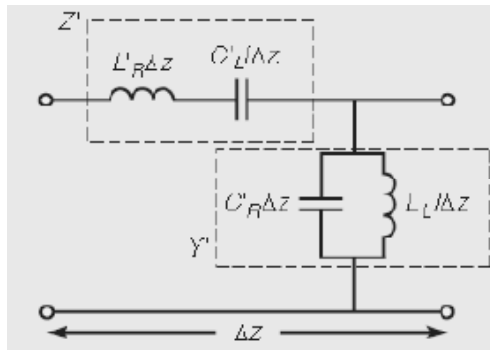


Figure 2.13: Lumped element equivalent circuit for CRLH TL.

The propagation constant of the above transmission line is given by;

$$\gamma = \alpha + j\beta = \sqrt{Z'Y'} \quad (2.20)$$

where per unit length impedance Z' and per unit length admittance Y' are;

$$Z' = j \left(\omega L'_R - \frac{1}{\omega C'_L} \right) \quad (2.21)$$

$$Y' = j \left(\omega C'_R - \frac{1}{\omega L'_L} \right) \quad (2.22)$$

Phase constant β is given by;

$$\beta = s \sqrt{\omega^2 L'_R C'_R + \frac{1}{\omega^2 L'_L C'_L} - \left(\frac{L'_R}{L'_L} + \frac{C'_R}{C'_L} \right)} \quad (2.23)$$

where,

$$s = \begin{cases} -1 & \text{if } \omega < \omega_{\Gamma 1} = \min \left(\frac{1}{\sqrt{L'_R C'_L}}, \frac{1}{\sqrt{L'_L C'_R}} \right) \\ +1 & \text{if } \omega < \omega_{\Gamma 2} = \max \left(\frac{1}{\sqrt{L'_R C'_L}}, \frac{1}{\sqrt{L'_L C'_R}} \right) \end{cases} \quad (2.24)$$

In equation 2.23, β can be purely real or purely imaginary depending on the sign of quantity inside the square root. Because of this behavior, the CRLH TL operates uniquely, characteristics only found in CRLH, not present in either RH or LH TL. When β is a pure real quantity, $\gamma = j\beta$ gives a pass band in the frequency range. In contrast, when β is imaginary, $\gamma = \alpha$ gives rise to a stop band in the frequency range. Figure 2.14 illustrates ω - β diagram of pure RH, pure LH and CRLH TL, respectively.

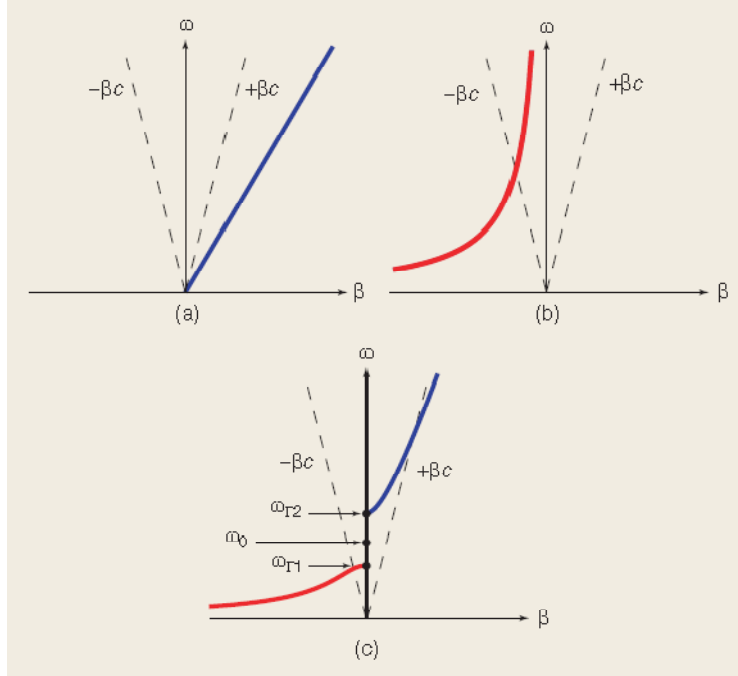


Figure 2.14: ω - β dispersion-attenuation diagram for (a) Pure RH (b) Pure LH, and (c) CRLH TL from equation 2.23. [21]

As a special case, when at a given frequency, series and shunt resonances are equal,

$$L'_R C'_L = L'_L C'_R \quad (2.24)$$

The circuit reduces to the circuit in the figure 2.15. At this frequency, CRLH is said to be balanced. Also, at this frequency, β becomes,

$$\beta = \beta_R + \beta_L = \omega \sqrt{L'_R C'_R} - \frac{1}{\omega \sqrt{L'_L C'_L}} \quad (2.25)$$

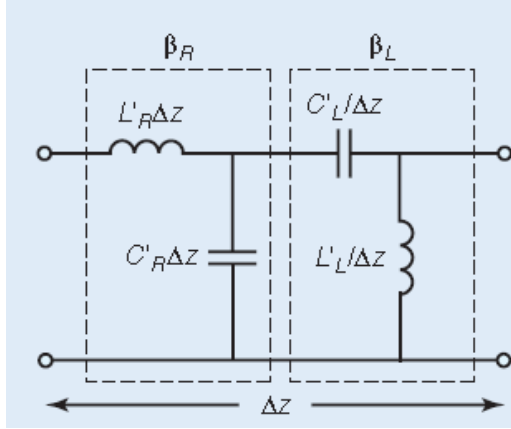


Figure 2.15: Equivalent circuit diagram of balanced CRLH.

At lower frequencies, CRLH is LH and at higher frequencies CRLH is RH as shown in figure 2.16. The frequency at which this transition occurs ω_0 is given by,

$$\omega_0 = \frac{1}{\sqrt[4]{L'_R C'_R L'_L C'_L}} = \frac{1}{\sqrt{L' C'}} \quad (2.26)$$

Unlike the unbalanced case, figure 2.16 shows that there is no stop band. Since $v_g \neq 0$ at ω_0 , there will be wave propagation, though $\lambda_g = 2\pi/|\beta|$ is infinite. However phase shift in such a line of length d is zero as $\phi = -\beta d = 0$. Phase advance occurs at frequencies below ω_0 and phase delay after it.

The transmission line can be related to constitutive parameters of CRLH as follows:

Characteristic impedance of the transmission line is given by,

$$Z_0 = \sqrt{\frac{Z'}{Y'}} \quad (2.27)$$

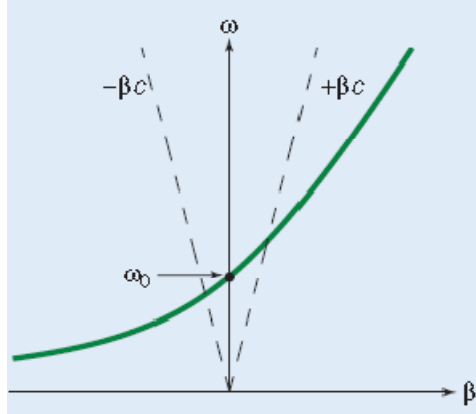


Figure 2.16: ω - β , dispersion-attenuation diagram of balanced CRLH.

Intrinsic impedance of a material is given by,

$$\eta = \sqrt{\frac{\mu}{\varepsilon}} \quad (2.28)$$

Propagation constant γ of the transmission line is,

$$\gamma = j\beta = \sqrt{Z'Y'} \quad (2.29)$$

Propagation constant of a material is,

$$\beta = \omega\sqrt{\varepsilon\mu} \quad (2.30)$$

$$Z_0 = \eta \rightarrow \frac{Z'}{Y'} = \frac{\mu}{\varepsilon} \quad (2.31)$$

Relation between constitutive parameters and characteristic impedance of the transmission line if as given below,

$$\varepsilon = \frac{Y'}{j\omega} = C'_R - \frac{1}{\omega^2 L'_L} \quad (2.32)$$

$$\mu = \frac{Z'}{j\omega} = L'_R - \frac{1}{\omega^2 C'_L} \quad (2.33)$$

The refractive index of the CRLH TL $n = c\beta/\omega$, for balanced and unbalanced line is shown in figure 2.17.

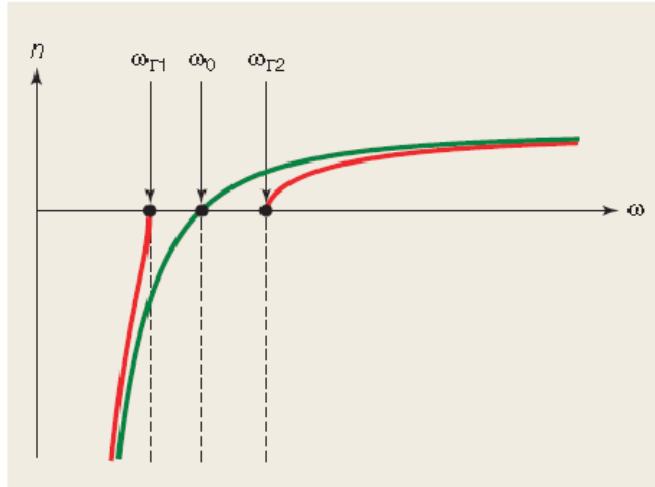


Figure 2.17: Refractive index of balanced (blue) and unbalanced (red) CRLH.

CHAPTER 3

WAVEGUIDE MINIATURIZATION USING ELECTROMAGNETIC METAMATERIALS

3.1 Introduction

Mathematical proof of wave propagation in circular and rectangular waveguides and the concept of cutoff frequency were given by Lord Rayleigh (John William Strutt) [22] in 1897. Before that, in 1893, Heaviside proposed wave propagation through closed hollow tubes, but his idea was rejected because of the belief that two wires were required for wave propagation [23]. Experimental verification of the circular and rectangular waveguides was made in 1932 and 1936 by George C. Southworth at AT&T and W. L. Barrow of MIT respectively. Waveguides have been used as guiding structures in antenna, radar, and microwave applications for over 70 years.

In the era of handheld, lightweight integrated micro devices, heavy bulky waveguides are being replaced by easily integratable planar guiding structures such as slot lines, micro strip, and coplanar lines. However there are certain applications, such as feeding networks for large antenna arrays, multifrequency antennas, certain radar applications, satellite communications, and broadcasting, where use of waveguide is almost necessary and unavoidable. Waveguide offers many advantages over coaxial or microstrip lines, viz., waveguides are completely shielded (excellent isolation from adjacent signals) have lower loss, and high power handling capability. Planar antennas such as patch antennas have disadvantages such as substrate mode losses, spurious radiation from feeding networks, and poor polarization purity. Owing to the three dimensional nature of waveguide antennas, they can be difficult to integrate with planar circuitry. The manufacturing costs of the waveguides are high because of the material and volume. The biggest disadvantage of waveguide however is its size and weight at low microwave frequencies. Considering the disadvantages, there is increased need for a compact, light weight, miniaturized waveguide working at low microwave frequencies.

3.2 Rectangular Waveguide

It is known from electromagnetics that for propagation of waves through a waveguide the width of the cross section of the waveguide must be at least one half of the wavelength as in equation 3.1 [1].

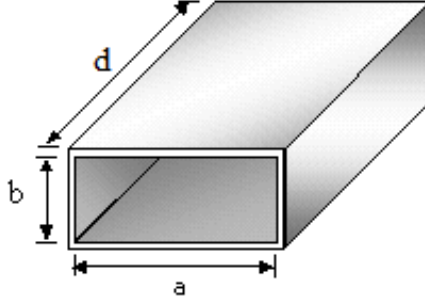


Figure 3.1: Rectangular waveguide.

$$\lambda_{cutoff} = 2a \quad (3.1)$$

$$f_{cutoff} = \frac{c}{2a} \quad (3.2)$$

A uniform waveguide of rectangular cross section with inner dimension $a \times b$ and length d is shown in figure 3.1. For waveguide walls made of finite conductivity material, the mode propagation constant $\gamma = \alpha + j\beta$ is complex. Attenuation constant α and wave number β depend on the cross section dimensions a and b , conductivity, and excitation wavelength λ . The cutoff wavelength and frequency of TE and TM modes is given by,

$$\lambda_{cutoff} = \frac{2}{\sqrt{\left(\frac{m}{a}\right)^2 + \left(\frac{n}{b}\right)^2}} \quad (3.3)$$

$$f_{cutoff} = \frac{1}{2\pi\sqrt{\mu_0\epsilon_0}} \sqrt{\left(\frac{m\pi}{a}\right)^2 + \left(\frac{n\pi}{b}\right)^2} \quad (3.4)$$

where a is inside width,

b is inside height,

m is number of half - wavelength variations of field in a direction,

n is number of half - wavelength variations of field in b direction,

ϵ_0 is free space permittivity,

μ_0 is free space permeability.

Guide wavelength is defined as the distance between two equal - phase planes along the waveguide. The guide wavelength depends on operating wavelength and the cutoff wavelength, and is always longer than the wavelength in free-space and is given by,

$$\lambda_{guide} = \frac{c}{f} \frac{1}{\sqrt{1 - \left(\frac{c}{2af}\right)^2}} \quad (3.5)$$

3.3 Miniaturization

The classical method of waveguide miniaturization is filling the waveguide with a dielectric [2]-[5]. Their size, relative to empty waveguide, is reduced by a factor of $1/\sqrt{\epsilon_r}$, where ϵ_r is the dielectric constant. Air - filled waveguides have a lower loss than the equivalent dielectric - filled waveguides. Recently ceramic dielectrics with high Q and high dielectric constants ranging from 20 to 90 have been developed. However such high - ϵ_r , dielectric - filled waveguides cannot radiate efficiently from the open end as the end wall act as a near perfect magnetic wall, which makes it unusable in antenna applications.

After electromagnetic metamaterials came into main - stage research, application of such materials supporting backward waves in guiding structures were studied by a number of researchers [6]-[8], [24]-[28]. Recently a very unusual waveguide was filled with Split - Ring Resonators (SRR) proposed by Marques *et al.* in [7] and then extensively studied by Hrubar *et al.* in [8].

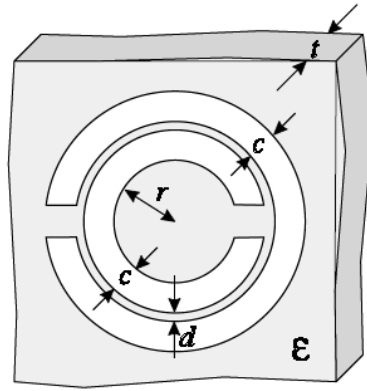


Figure 3.2: The split - ring resonator (SRR) geometry used in [7].
 $r = 1.4 \text{ mm}$, $c = 0.5 \text{ mm}$, $d = 0.2 \text{ mm}$, $t = 0.49 \text{ mm}$, $\epsilon = 2.43\epsilon_0$.

In Marques *et al.*'s work, SRR geometry shown in figure 3.2 is located periodically in the symmetry plane of a square cross section waveguide as shown in figure 3.3. The system forms a metamaterial medium of unit cell size of 6 mm .

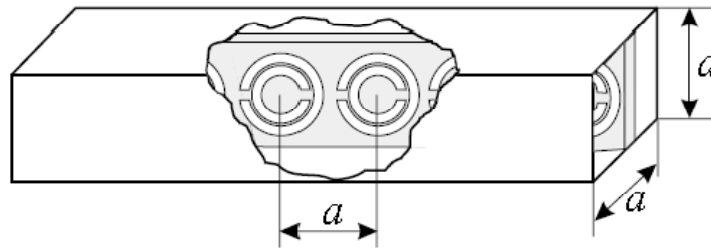


Figure 3.3: The split - ring resonator (SRR) loaded square cross section waveguide
 $(a = 6 \text{ mm})$ [7].

The cut off frequency of the waveguide is 25 GHz ($6\text{ mm} \times 6\text{ mm}$). Due to the presence of SRR inside the square waveguide, around the resonant frequency of the SRR the effective permittivity of the medium becomes negative, supporting backward waves. The SRR – loaded square waveguide was placed in between two sections of C – Band rectangular waveguide fed with coaxial lines as shown in the figure 3.4.

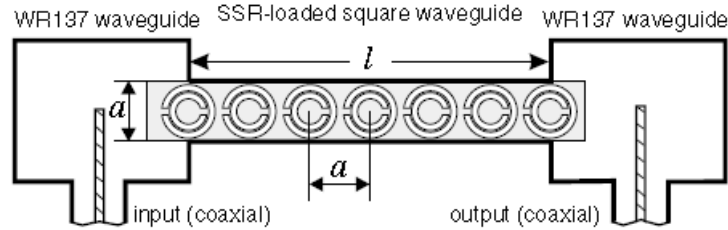


Figure 3.4: Experimental setup used in [7] ($l = 36\text{ mm}$)

The measured transmission coefficient (S_{12}) for the square waveguide with $l=36\text{ mm}$ and loaded with 7 SRR's is shown in figure 3.5. Clearly, as seen in figure 3.5, transmission occurs around 6 GHz, well below the cutoff frequency of the waveguide (25 GHz), even though the loss is very high ($\approx 20\text{ dB}$).

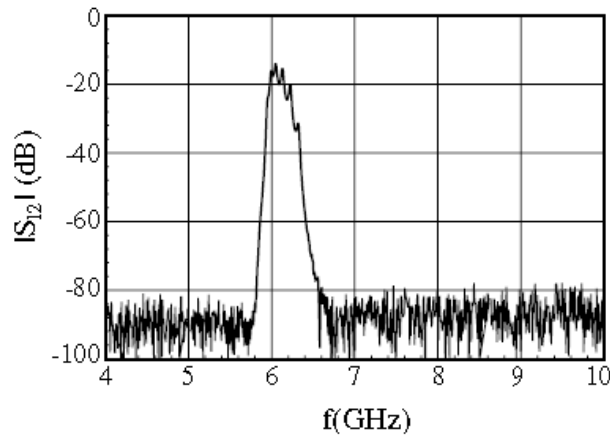


Figure 3.5: Transmission coefficient (S_{12}) as reported in [7] ($l = 36\text{ mm}$).

The analysis of the SRR – loaded waveguide is based on effective homogeneous medium when the unit cell size ' a ' of the medium is much smaller than the guided

wavelength λ_g ($a \ll \lambda_g$). Considering the unit cell of size ‘ a ’ in figure 3.3, the single SRR can be thought of a capacitively loaded loop antenna as shown in figure 3.6 [29]. The radius of the loop is considered to be much smaller than the wavelength of the incident field. The narrow split in the ring can be thought as a loading capacitor of impedance ‘ Z ’. When such a structure is illuminated by a plane wave with magnetic field intensity H_i , the perpendicular vector of the magnetic field induces a current in the loop given by;

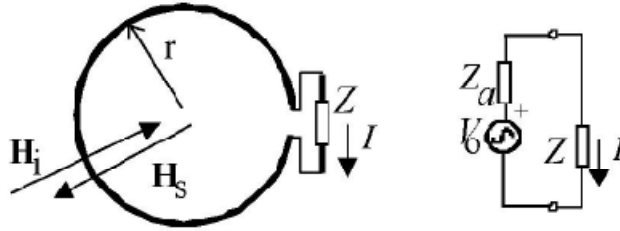


Figure 3.6: Capacitively loaded loop antenna and equivalent circuit diagram [29].

$$I = \frac{V_0}{Z_a + Z} = \frac{-j\omega\mu_0 A H_i}{Z_a + Z} \quad (3.6)$$

where Z_a is the impedance of antenna loop,

Z is the load capacitance,

A is the loop area,

ω is the angular frequency of incident field,

μ_0 is the free space permeability.

The current flowing in the loop produces a new magnetic field which causes scattering in the opposite direction of the original plane wave. The scattered magnetic field is given by;

$$H_s = KI \quad (3.7)$$

where K is a constant depending on the geometry of the system.

The resultant magnetic field is sum of scattered and incident fields,

$$H = H_i + H_s = H_i \left[1 - j \frac{K\omega\mu_0 A}{Z_a + Z} \right] \quad (3.8)$$

The inductive nature of the loop and the loading capacitance give rise to resonant behavior. The resultant field will be,

$$H = H_i \left[1 - j \frac{K\omega\mu_0 A}{R + j\omega L - \frac{1}{j\omega C}} \right] \quad (3.9)$$

where R , L and C are resistance, inductance, and capacitance of the loop circuit respectively.

Slightly above the resonance of the structure the scattered field H_s will be almost out of phase with the incident field H_i , yielding lower local resultant field. This will result in negative polarization and negative effective permeability given by [8], [13], [30],

$$\mu_{eff} = \mu'_{eff} - j\mu''_{eff} = 1 - \frac{f_{mp}^2 - f_0^2}{f^2 - f_0^2 - j\gamma f} \quad (3.10)$$

where f is the frequency of the incident wave,

f_{mp} is the magnetic plasma frequency (when $\mu_{eff} = 0$),

f_0 is the resonant frequency of SRR (when μ_{eff} diverges),

γ is the loss factor.

f_{mp} and f_0 are dependent on lattice constant and geometry of the SRR [13].

When the magnetic field vector of incident plane wave is perpendicular to the SRR (x direction), it will induce a current in the rings yielding negative permeability (refer to figure 3.7). On the other hand, the parallel components of the magnetic vector cannot induce any current in the rings.

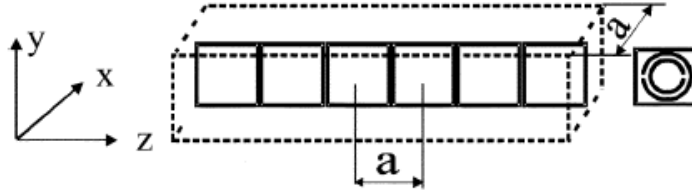


Figure 3.7: Square waveguide filled with SRR [8].

So components in both parallel directions (y and z directions) of the rings cannot affect the permeability leaving it equal to that of vacuum ($\mu_{pr} = 1$). So, the filling shown in figure 3.7 gives rise to uniaxial metamaterial with a permeability given by,

$$\bar{\mu} = \mu_0 \begin{bmatrix} \mu_{tr} & 0 & 0 \\ 0 & \mu_{pr} & 0 \\ 0 & 0 & \mu_{pr} \end{bmatrix} = \mu_0 \bar{\mu}_r \quad (3.11)$$

where μ_0 is the permeability of free space,

μ_{tr} is relative permeability in x direction (transverse),

μ_{pr} is relative permeability in y and z directions (parallel).

Since μ_{pr} appears in both y and z directions, μ_{pr} can be written as μ_{lr} (longitudinal) and the tensor can be reduced to 2×2 matrix,

$$\bar{\mu} = \mu_0 \begin{bmatrix} \mu_{tr} & 0 \\ 0 & \mu_{lr} \end{bmatrix} = \mu_0 (\bar{\mu}'_r - j \bar{\mu}''_r) = \mu_0 \bar{\mu}_r \quad (3.12)$$

The wave equation for the waveguide in figure 3.7 is given by [8],

$$\nabla \times \bar{\mu}_r^{-1} (\nabla \times \vec{E}) = k_0^2 \epsilon_r \vec{E}, \quad k_0^2 = \omega^2 \mu_0 \epsilon_0 \quad (3.13)$$

where \vec{E} is electric field,

k_0 is free space propagation constant,

ϵ_0 is free space permittivity,

ϵ_r is relative permittivity of the medium.

Assuming that the waveguide supports the TE mode, the dispersion equation can be written as [8],

$$\frac{k_x^2}{\mu_{lr}} + \frac{k_z^2}{\mu_{lr}} = \epsilon_r k_0^2 \quad (3.14)$$

From equation 3.14, the longitudinal propagation constant is given by,

$$k_z = \pm \sqrt{\epsilon_r \mu_{lr} \left(k_0^2 - \frac{k_x^2}{\epsilon_r \mu_{lr}} \right)} = \beta_z - j\alpha_z \quad k_x = \frac{m\pi}{a} \quad m = 1, 2, 3, \dots \quad (3.15)$$

where a is the width of the waveguide,

k_x is the propagation factor in transverse direction,

k_z is the propagation factor in longitudinal direction,

β_z is the phase constant,

α_z is the attenuation constant.

Depending on the solution of the root term, there can be two possible values for the propagation constant k_z . Since the flow of energy must decay from the source, the meaningful solution occurs when $\alpha_z > 0$. Considering a lossless material for the rings ($\epsilon_r'' = \mu_r'' = 0$), the longitudinal propagation constant in equation 3.15 can be written as,

$$k_z = \pm k_0 \sqrt{\epsilon_r \mu_{lr} \left[1 - \left(\frac{f_c}{f} \right)^2 \right]} = \beta_z \quad f_c = \frac{f_{c0}}{\sqrt{\epsilon_r \mu_{lr}}} \quad f_{c0} = \frac{mc}{2a} \quad (3.16)$$

where f is the frequency of the incident wave,

f_{c0} is the cutoff frequency of the empty waveguide,

f_c is the cutoff frequency of the waveguide with filling.

The effect of filling material in the waveguide is shown in the figure 3.8 [8].

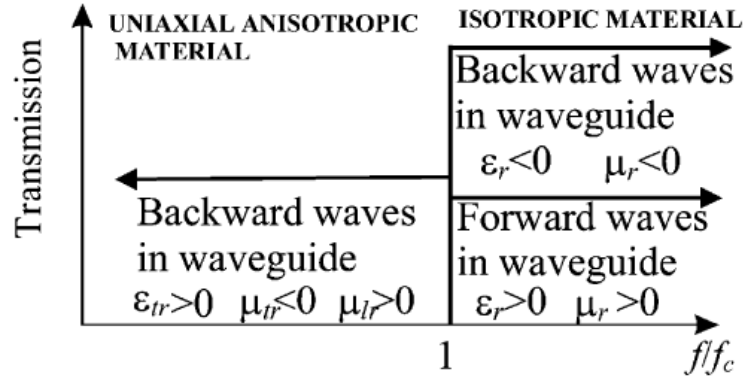


Figure 3.8: Effect of filling material in the waveguide.

One can clearly notice, filling of the uniaxial anisotropic metamaterial with negative transverse permeability, waveguide can support backward wave below cutoff frequency of the waveguide. This kind of waveguide exhibits lowpass behavior, and it can be seen as the dual of ordinary waveguide with highpass behavior.

The bandwidth of the backward wave propagation is governed by the dispersion property of the material filling. In the discussion above, we have considered material with no dispersion. In nature, every material has dispersion. Therefore, the material filling can support backward wave propagation only within the limited frequency band.

Above waveguide can also be analyzed with the help of transmission line theory [8]. The waveguide can be modeled as simple two wire TEM transmission line with infinite number of short circuited shunt stuns of length $a/2$, as shown in figure 3.9.

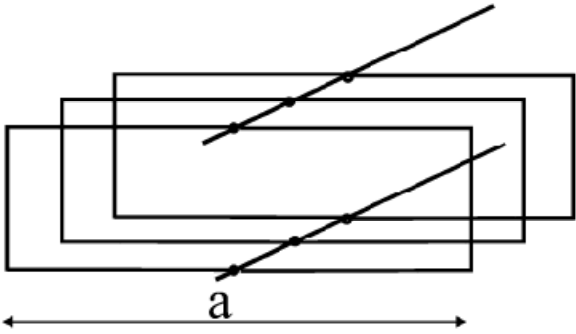


Figure 3.9: Transmission line representation of a rectangular waveguide [8].

Further as shown in figure 3.10, the transmission line can be modeled as distributed series inductance associated with transverse permeability (μ_t). The distributed capacitance can be modeled due to presence of metamaterial filling permeability (ϵ).

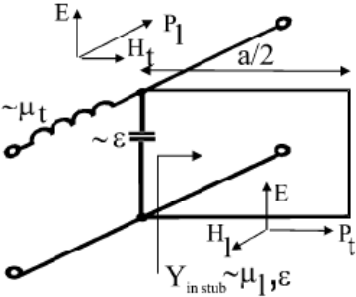


Figure 3.10: Inductance and capacitance model of figure 3.7 [8].

Energy flow in the shunt stub induces longitudinal magnetic field H_l and it introduces a distributed shunt inductance. Figure 3.11 shows the modeled equivalent circuit.

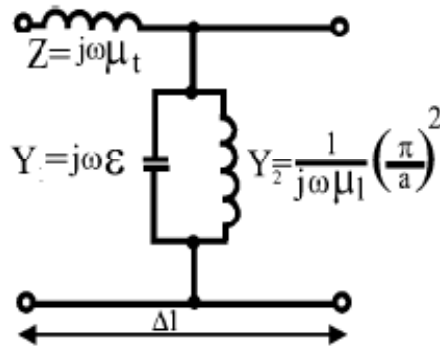


Figure 3.11: Equivalent circuit of a waveguide filled with uniaxial material [8].

Wave impedance of the equivalent circuit shown in figure 3.11 can be written as,

$$Z_w = \pm \sqrt{\frac{Z}{Y_1 + Y_2}} = \pm \sqrt{\frac{\mu_0 \mu_r}{\epsilon_0 \epsilon_r \left[1 - \left(\frac{f_c}{f_0} \right)^2 \right]}} \quad f_c = \frac{f_{c0}}{\sqrt{\epsilon_r \mu_r}} \quad (3.17)$$

When the filling in the waveguide is uniaxial anisotropic material, transversal relative permeability is negative. When the incident wave frequency is below cutoff frequency of the waveguide ($f < f_c$), shunt stub will be shorter than a quarter wavelength, shunt tank circuit in figure 3.11 operates below cutoff frequency and behaves as inductive element. This gives rise to series C shunt L line discussed in chapter 2 which supports backward waves. Effect of different filling in the waveguide is listed in table 2.1 [32].

Table 3.1: Effect of different filling in the waveguide.

| Type of filling in the waveguide | μ_r | ϵ_r | Type of resulting Transmission line (Series and shunt elements) | |
|----------------------------------|--|------------------|---|---------------------------------|
| | | | $f < f_c$ | $f > f_c$ |
| Isotropic DPS | $\mu_{rl} = \mu_{rt} = \mu_r$ $\mu_r > 0$ | $\epsilon_r > 0$ | L – L (No propagation) | L – C (Forward propagation) |
| Isotropic ENG | $\mu_{rl} = \mu_{rt} = \mu_r$ $\mu_r > 0$ | $\epsilon_r < 0$ | L – L (No propagation) | L – L (No propagation) |
| Isotropic MNG | $\mu_{rl} = \mu_{rt} = \mu_r$ $\mu_r < 0$ | $\epsilon_r > 0$ | C – C (No propagation) | C – C (No propagation) |
| Isotropic DNG | $\mu_{rl} = \mu_{rt} = \mu_r$ $\mu_r < 0$ | $\epsilon_r < 0$ | C – C (No propagation) | C – L (Backward propagation) |
| Uniaxial MNG | $\mu_{rl} > 0$ $\mu_{rt} < 0$ | $\epsilon_r > 0$ | C – L (Backward propagation) | C – C (No propagation) |

Various geometries of Uniaxial MNG have been studied by several researchers. The driving criteria behind optimizing geometries have been to reduce the losses in the resulting medium, to increase the bandwidth of the negative properties, to reduce the anisotropy, and to reduce the electrical size so that a compact medium can be built. Some of the geometries studies are, edge side coupled SRR (circular and square) [12], [30], broadside coupled SRR (square and circular) [33], axially symmetric SRR [34], omega SRR [35], [36], and the S ring [37]. R. Marques et al. studied a detailed comparative analysis of Edge coupled and broadside coupled SRR's in [38]. Their research revealed a number of advantages of broadside coupled SRR (figure 3.12) over edge coupled SRR, viz. broad side coupled SRR gives better symmetry cancelling bi-anisotropy of edge

coupled SRR, broadside coupled SRR has potentially much smaller electrical size which helps in designing discrete metamaterial with smaller cell size and such structure has much higher mutual capacitance reducing the resonant frequency of the inclusion.

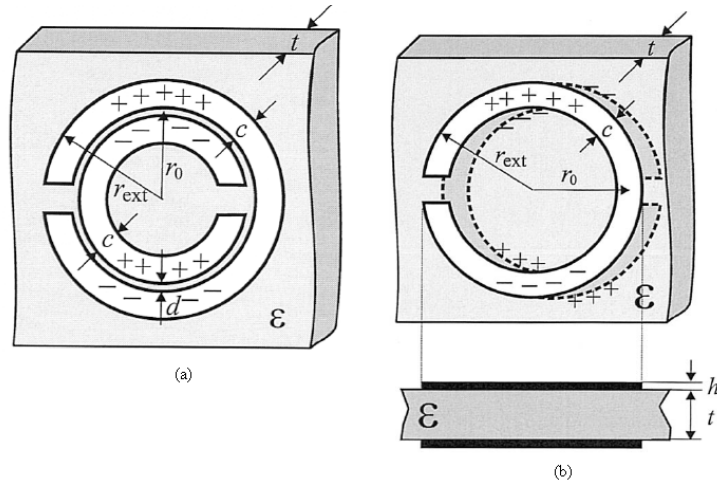


Figure 3.12: Broadside coupled SRR.

Considering this, in the design of open - ended miniaturized waveguide antenna, we will use broadside coupled SRR loading in the symmetry plane of an x-band waveguide.

All previous research efforts made with electromagnetic metamaterials, were in miniaturizing the waveguides as guiding structures. This thesis focuses on extending that to a miniaturized waveguide antenna radiating below the cutoff frequency of the waveguide. Design, simulation, and experimental results of such an antenna are presented in the following chapters.

CHAPTER 4

THEORETICAL INVESTIGATIONS AND SIMULATIONS

4.1 Introduction

Most of the techniques described to analyze electromagnetic structures can become complex. In many cases, an exact solution may not be possible. The Ansoft High Frequency Structure Simulator is an interactive software package for calculating the electromagnetic behavior of a structure including post-processing commands in detail. Ansoft HFSS™ is the industry-standard software for S-parameter, Full-Wave SPICE extraction, basic electromagnetic field quantities, and, for open boundary problems, radiated near and far fields, characteristic port impedances and propagation constants, generalized S-parameters and S-parameters renormalized to specific port impedances, eigenmodes, or resonances, of a structure and 3D electromagnetic field simulation of high-frequency and high-speed components. Engineers rely on the accuracy, capacity, and performance of HFSS to design on-chip embedded passives, IC packages, PCB interconnects, antennas, RF/microwave components, and biomedical devices. The EM simulator characterizes full wave and radiative effects for multi-layered structures.

This chapter focuses on theoretical investigation of the compact waveguide antennas using electromagnetic metamaterials. A 3D EM structure simulator, Ansoft HFSS used to simulate the antennas designed in this thesis. Chapter also provides an insight into the various aspects involved in the process of modeling and running simulations.

4.2 Ansoft HFSS™ FEM method

HFSS™ utilizes a 3D full-wave Finite Element Method (FEM) to compute the electrical behavior of high-frequency and high-speed components. With HFSS one can extract parasitic parameters (S, Y, and Z), visualize 3D electromagnetic fields (near- and

far-field), and generate Full-Wave SPICE models to evaluate signal quality effectively, including transmission path losses, reflection loss due to impedance mismatches, parasitic coupling and radiation. HFSS features new higher-order, hierarchical basis functions combined with an iterative solver that provides accurate fields, smaller meshes and more efficient solutions for large multi-wavelength structures. A new fault tolerant, high-quality finite element meshing algorithm further enhances HFSS's ability to simulate very complex geometric models, including models imported from 3D CAD environments. HFSS is dynamically linked with Nexxim® and Ansoft Designer® to create a powerful electromagnetic-based design flow. This design flow enables users to combine complex, highly nonlinear circuits with transistor-level detail and 3D full-wave accurate component models to solve challenging high-performance electronic designs. HFSS™ includes a 3D ACIS-based solid-modeling tool to create 3D models of waveguides, antennas, connectors, packages and more. Users have the option of performing quick pre-layout diagnostics and design variations using the HFSS drawing tool and/or importing existing designs through AnsoftLinks™ (Cadence, Mentor Graphics, Synopsys, Zuken and CAD files such as DXF, GDSII, Pro/E, Catia, STEP, and IGES). The resulting S-parameter and/or Full-Wave SPICE™ models can then be taken into circuit tools such as Ansoft Designer®, DesignerSI™, Nexxim® or other SPICE/RF tools for additional circuit and system simulations.

The finite-element solver in HFSS divides the entire structure into a finite number of elements (triangles and rectangles), a process called meshing. Solution accuracy depends on the size of individual elements. The finer the elements are, the more accurate is the solution. There is a tradeoff between size of the element and computing resource available. For a large structure, finer mesh means a large number of elements which requires a large amount of computer memory and processing capability. Therefore, care should be taken while choosing the mesh size so that it is not too coarse to compromise the accuracy of the solution and not too fine to overwhelm the available computing resources. To generate fairly accurate solution, the mesh size should be smaller than a quarter wavelength of the wave of excitation.

To optimize the mesh size, HFSS refines the mesh iteratively in the area of the highest error, at the solution frequency. In the first iteration HFSS generates a solution based on an initial mesh. It checks the solution accuracy to a user defined value. If error tolerance is not met, it refines the mesh in critical areas and generates a new solution. When the error tolerance converges to a user defined precision, HFSS breaks out of the loop. Also, the maximum number of iterations can be set to a pre defined number. When this number is reached even though the error has not converged, HFSS breaks the loop with a warning indicating error not converged.

The above mesh refinement happens at the solution frequency selected. As an alternative, a fixed-densy mesh definition can be used at a frequency near the high end of the sweep range. The mesh generated using this option is more uniform and accurate than automatic mesh refinement. The advantage of the fixed density-mesh over the adaptive mesh is that no extra simulations are needed to generate the mesh before the frequency sweep can be done.

4.3 Getting Started with HFSS

The HFSS desktop consists of several windows, a menu bar, toolbars, and a status bar as shown in figure 4.1 to help navigate and control the project.

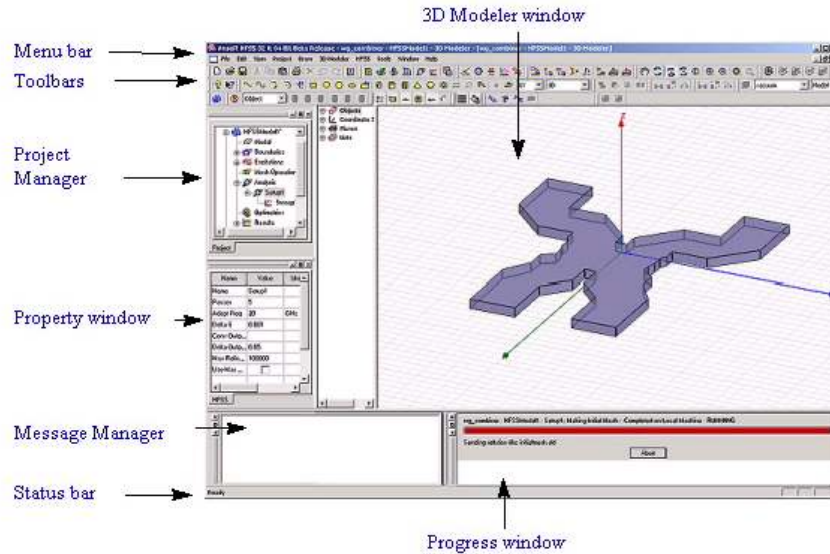


Figure 4.1: HFSS Desktop with interactive menu and tool bars.

The menu bar enables you to perform all HFSS tasks, such as managing project files, customizing the desktop, drawing objects, and setting and modifying all project parameters with numerous menu items. The toolbar buttons and shortcut pull-down lists act as shortcuts for executing various commands. To execute a command, you click a toolbar button or click a selection on the shortcut pull-down list. The Project Manager window displays the open project's structure, which is referred to as the project tree. The Project Manager window displays details about all open HFSS projects. Each project ultimately includes a geometric model, its boundary conditions and material assignments, and field solution and post-processing information. The Properties window displays the attributes, or properties, of an item selected in the project tree, the history tree, or the 3D Modeler window. The Properties window enables you to edit an item's properties. The properties, and the ability to edit them in the Properties window, will vary, depending on the type of item selected. The tabs available in the Properties window will also vary, depending on the selection. The Message Manager displays messages associated with a project's development, such as error messages about the design's setup or informational messages about the progress of an analysis. The status bar is located at the bottom of the application window. It displays information about the command currently being

performed. The Progress window monitors a simulation while it is running. Finally, after you insert an HFSS design into the current project, you can draw a model of the electromagnetic structure. The general strategy is to build the model as a collection of 3D objects. Each material type is treated as a separate object. HFSS lets the user to create 3D objects by using HFSS's Draw commands or by drawing 1D and 2D objects, and then manipulate them to create 3D objects. Objects are drawn in the 3D Modeler window. The user can also import objects from other systems or CAD drawing packages.

4.4 Optimization

Before we arrived at the waveguide antenna presented in this thesis, we investigated a number of other ring structures through simulation, shown in figure 4.2.

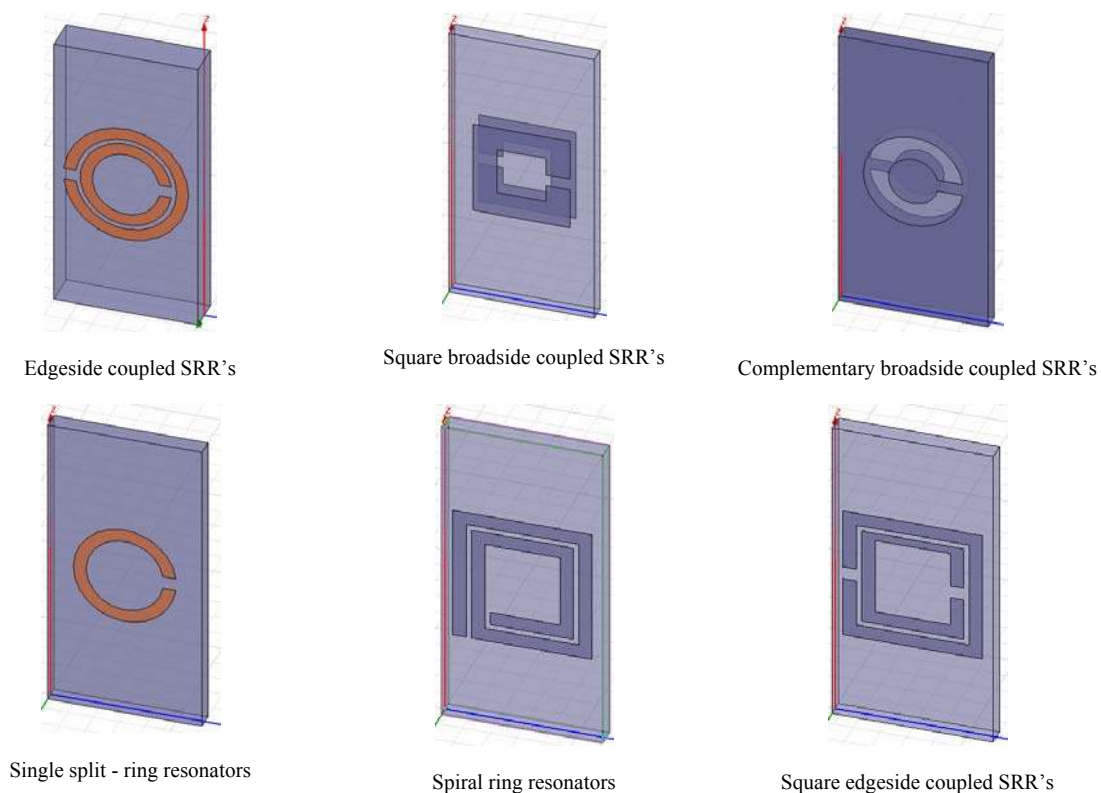


Figure 4.2: Different structures tried for antenna miniaturization.

Some of the structures tried were, edgeside coupled SRR's, square broadside coupled SRR's, complementary broadside coupled SRR's, single split - ring resonators, spiral ring resonators, and square edgeside coupled SRR's. After considering different inclusions, the antenna was optimized with BC-SRR. To keep the report precise, we will focus only on the simulations involving BC – SRR. Following sections in this chapter present the theoretical results and simulation steps of proposed miniaturized waveguide antenna.

4.5.1 Project Design

As described in the previous chapter, based on the conclusion in [38], broadside coupled split - ring resonators (BC-SRR) are used as the inclusion in an X-band waveguide. In the simulations we assumed the rings were milled on a commercial 60 mil thick Roger's RT Duroid 5870 with relative permittivity of 2.33. The rings had an outer radius of 3 mm and inner radius of 2 mm. Slit width was set to 0.5 mm. Left - handed medium is simulated by a regular array of twelve BC – SRR's placed in the symmetry plane of 60 mm long X – band waveguide (cutoff frequency 6.6 GHz). The spacing between the rings is set to 6 mm. The X – band waveguide loaded with SRR is excited by a C – band waveguide-to-coaxial transition (cutoff frequency 4.3 GHz). To ensure the excitation of the first SRR in the array, the first ring was partially placed out from the X – band waveguide; and to improve the radiation, the last ring was partially placed out from the open end of the waveguide along with an extra ring as shown in figure 4.3.

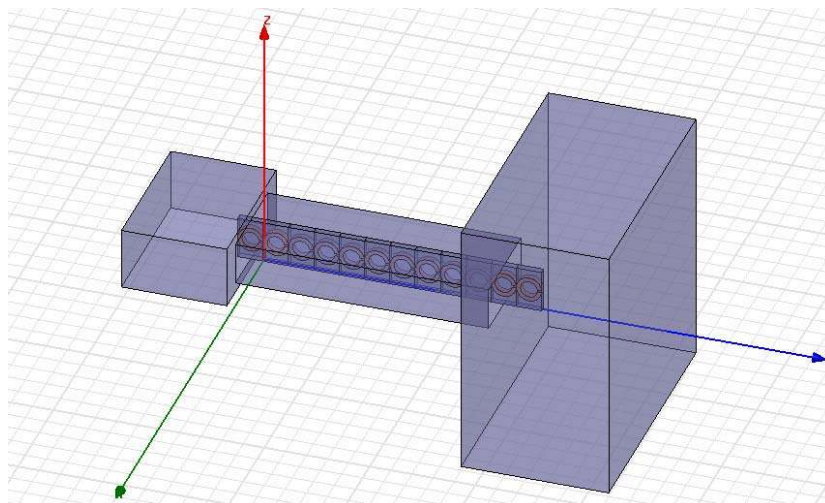


Figure 4.3: HFSS model of the setup.

This approach to excite the first ring by placing a ring partially out in C-Band waveguide and to facilitate the better radiation from open end by placing an extra ring was taken after we simulated different configurations like, rings flushed to X-Band waveguide, rings partially out in both C-Band waveguide and radiating end, one ring extra on each side, etc. Some of the simulations conducted are shown in figure 4.4 (a), 4.4 (b) and 4.4 (c). It is seen from the figures that either there is very little radiation below cutoff frequency of the waveguide or passband has a very small bandwidth.

To verify the conclusions of [38], a comparative study both E-SRR and BC-SRR loaded waveguide antenna was conducted.

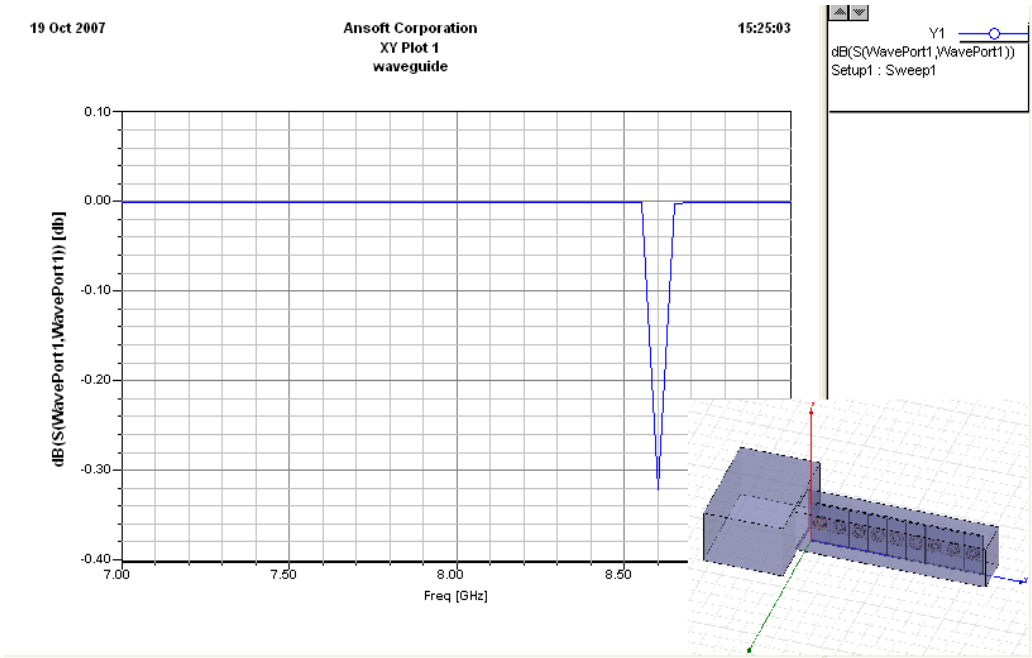


Figure 4.4 (a): Return loss for 9 rings placed in a waveguide of 60 mm long.

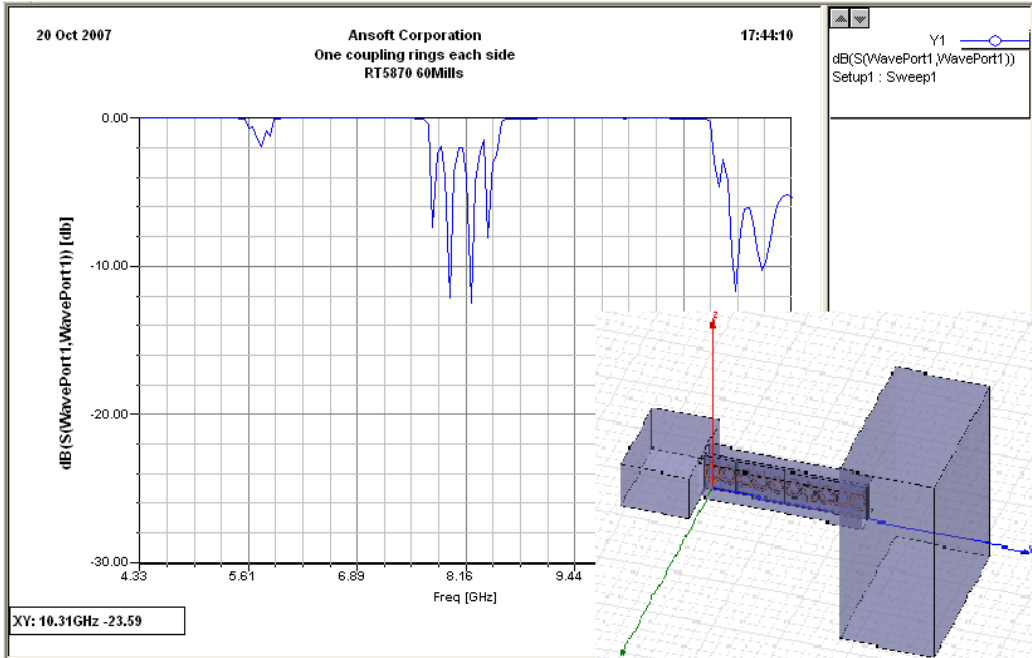


Figure 4.4 (b): Return loss for 10 rings placed in a waveguide of 60 mm long (flush).

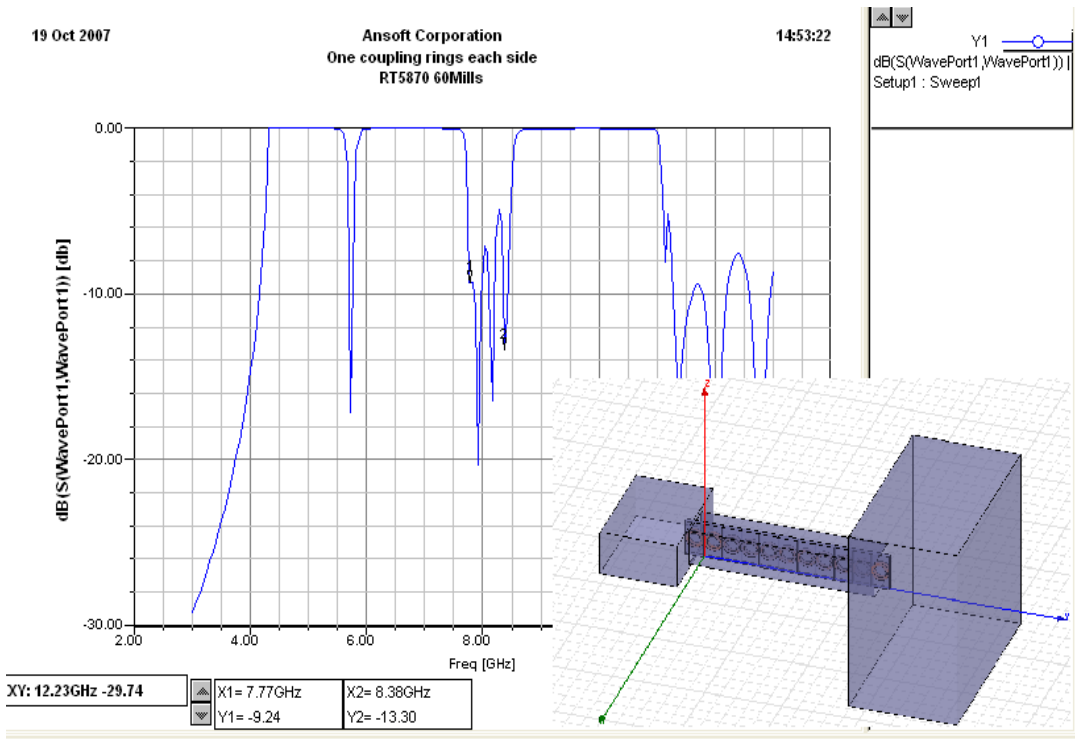


Figure 4.4 (c): Return loss for 11 rings placed in a waveguide of 60 mm long.

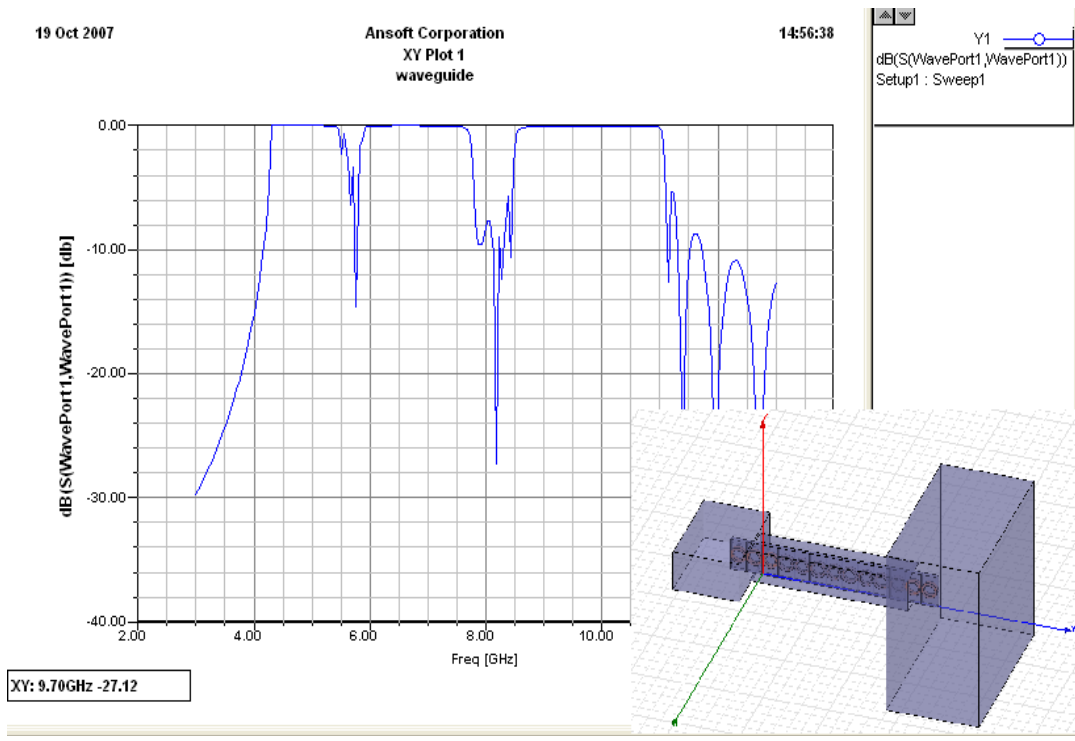


Figure 4.4 (d): Return loss for 13 rings placed in a waveguide of 60 mm long.

Similar setup in figure 4.3 was simulated with edgeside coupled SRR's loaded in the symmetry plane of the X-Band waveguide. Simulation model is shown in figure 4.5.

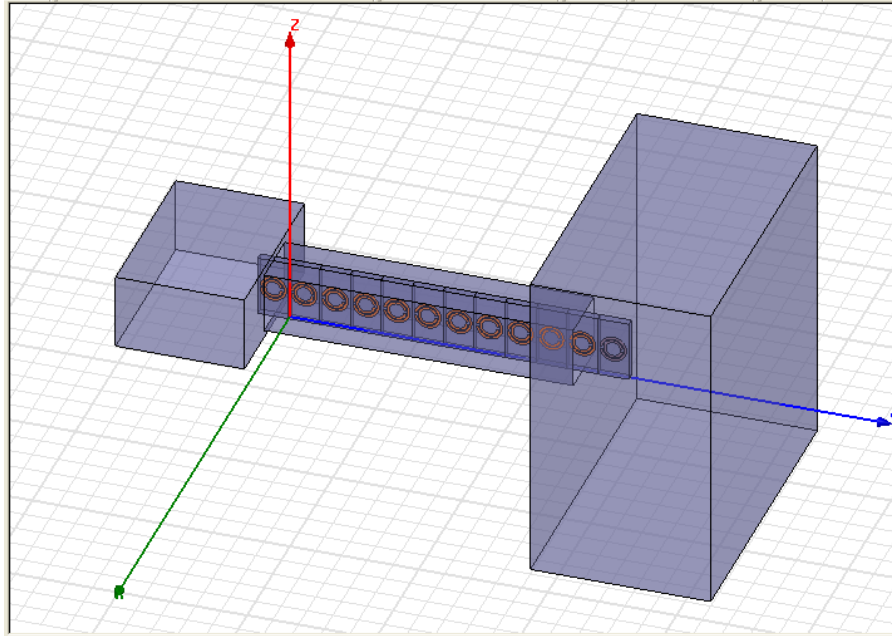


Figure 4.5: HFSS model of waveguide antenna with 13 E-SRR placed in symmetry plane.

Reflection coefficient (S_{11}) or return loss at the input port for the antenna is plotted as shown in figure 4.6.

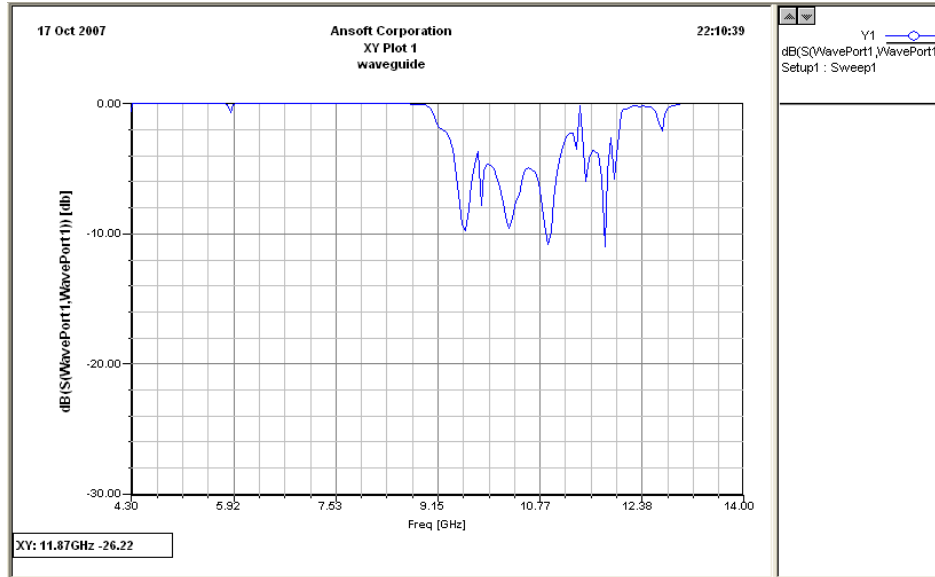


Figure 4.6: Return loss for the E-SRR loaded waveguide antenna.

From the plot, one can notice, at 5.9 GHz the antenna tries to radiate but only with very high return loss.

4.5.2 HFSS model Setup

In HFSS a project is said to be the collection of one or more design saved in an .hfss file. When HFSS is opened, a new default project is already open as shown in figure 4.7. The default design name in the project manager can be changed to desired name. The 3D modeler window appears by clicking on the design (figure 4.7).

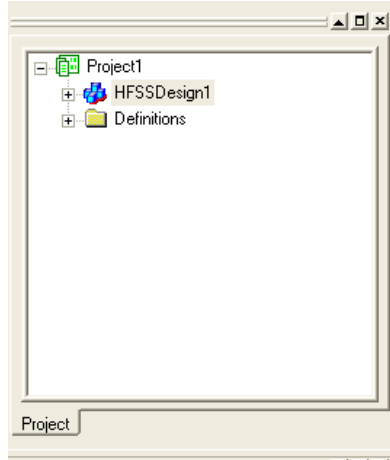


Figure 4.7: HFSS project manager.

Setting up the design for analysis depends on the solution desired. In this design for calculating the mode-based S-parameters of a passive waveguide that is driven by a source, the appropriate solution type is Driven Modal. The Driven modal solution is selected from HFSS solution Type menu. From the 3D modeling menu, the unit of measurement for drawing is set to 'mm' as shown in figure 4.8.

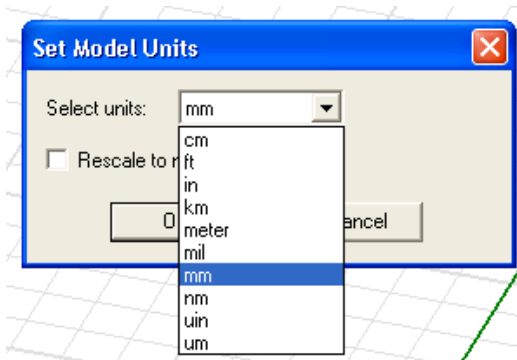


Figure 4.8: Selecting unit of measurement for drawing.

First, a box of 1.524 mm x 6 mm x 10.16 mm is drawn from the tool menu to represent a unit cell substrate. A property window appears, enabling you to change the position, name, color, transparency, material, etc. (figure 4.9). Default material assigned to box is

‘vacuum’. By clicking on the Material button in Attribute tab, the material is changed to Rogets RT Duroid 5870. On this box, circle of 3 mm and 2 mm diameter are drawn. By subtracting these two circles using the Boolean command in 3D modeler menu, the required trace of 1 mm thick is obtained.

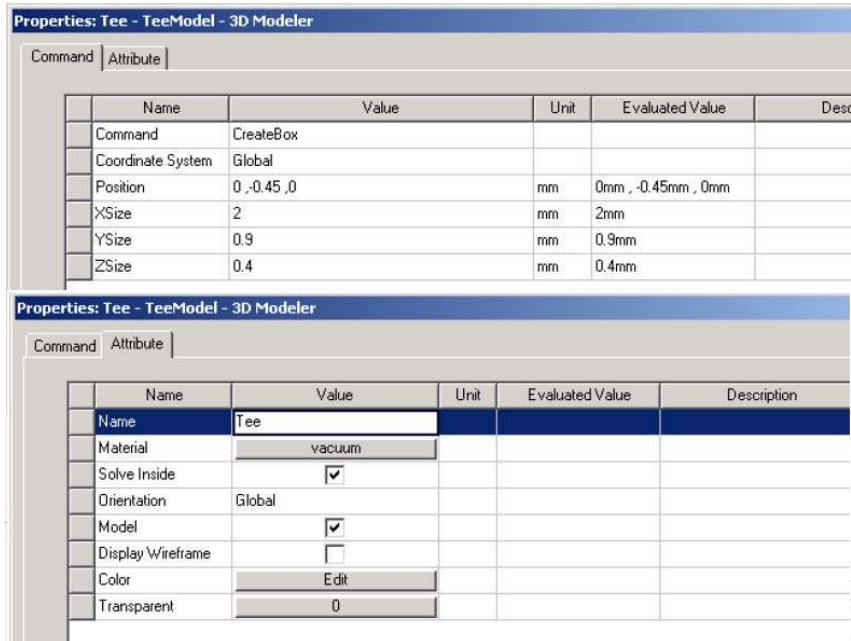


Figure 4.9: Property window.

To create the slit in the ring, a rectangle of 0.5 mm is drawn and subtracted similarly (figure 4.10).

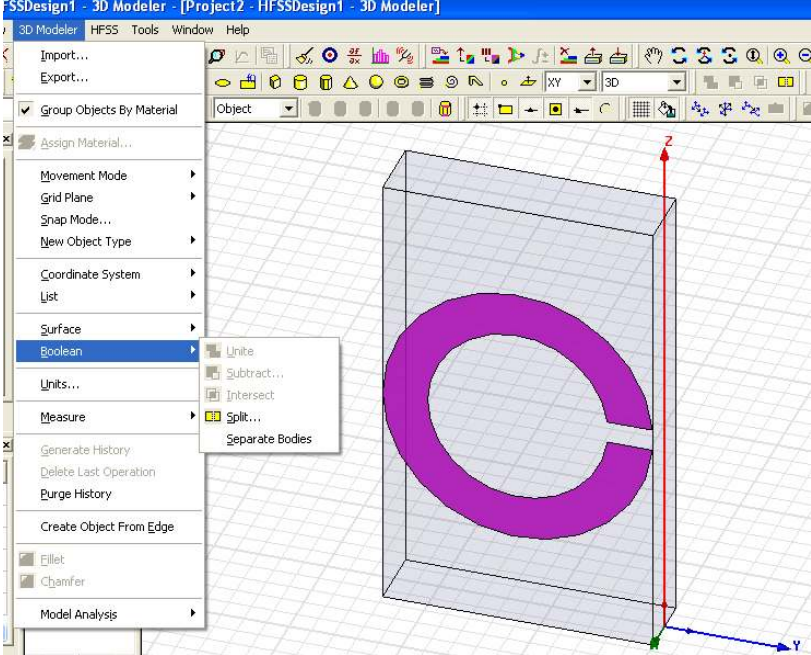


Figure 4.10: Unit cell.

By using ‘Duplicate Mirror’ command, the trace on the opposite side of the substrate is drawn (figure 4.11).

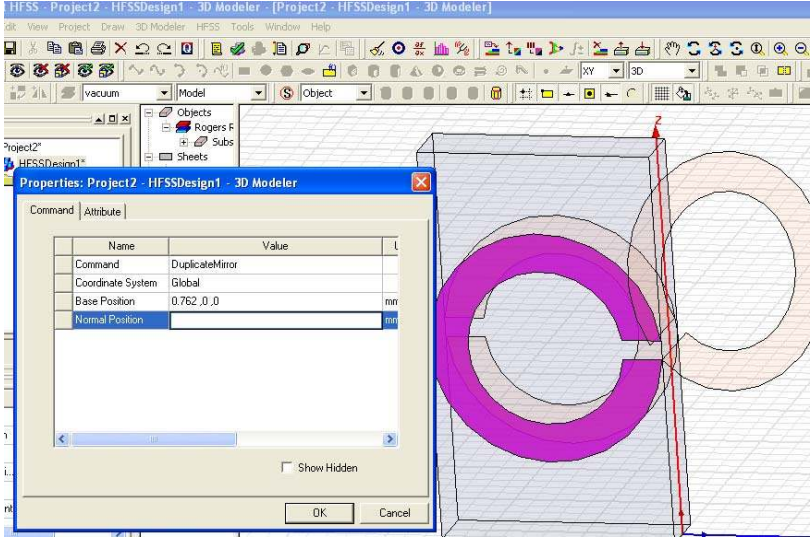


Figure 4.11: Duplicate along axis command.

The entire structure is selected and duplicated along the line to create twelve unit cells as required (figure 4.12).

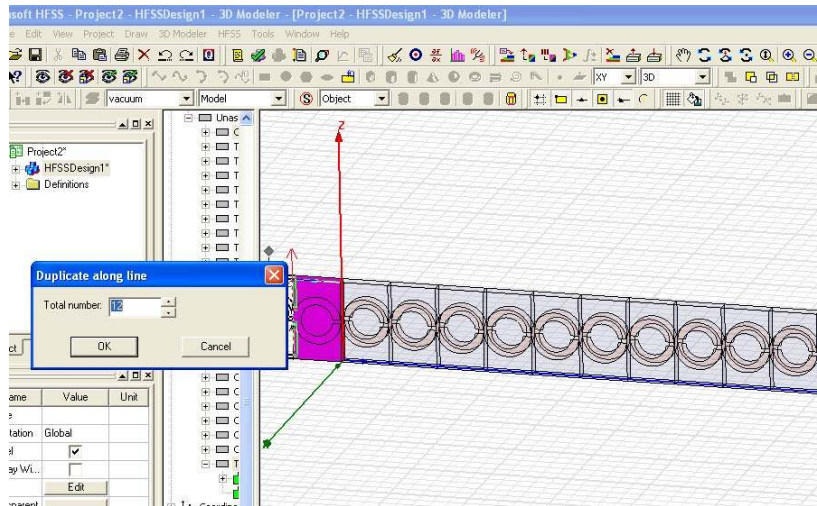


Figure 4.12: Array of twelve BC-SRR's.

On this structure, waveguides are drawn by creating boxes of required size (35 mm x 25 mm x 15 mm for C – band, 22.86 mm x 60 mm x 10.16 mm for X - band). Air box is drawn at the open end of the waveguide to simulate the radiation boundary. The final simulation setup is shown in figure 4.3.

4.5.3 Assigning excitation and boundary

After completing the drawing, an excitation wave port is placed on face of the C-band waveguide parallel to the yz plane is selected. By right clicking on the face and selecting the 'Assign Excitation' option, the wave port is assigned to the face (figure 4.13). As a part of the set up process, an integration line, which is a vector that specifies the direction of the excitation field pattern at the port is defined.

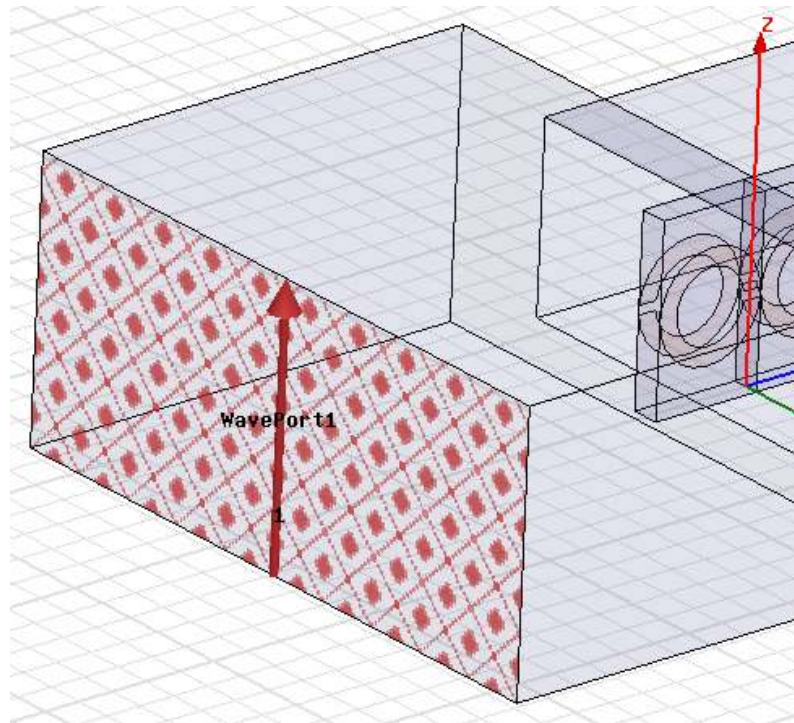


Figure 4.13: Wave port assignment.

Now the structure is ready to assign boundary conditions. All the metal parts (waveguide walls and rings) are selected and assigned 'Perfect E' boundary by right clicking and selecting 'Assign Boundary' option (figure 4.14).

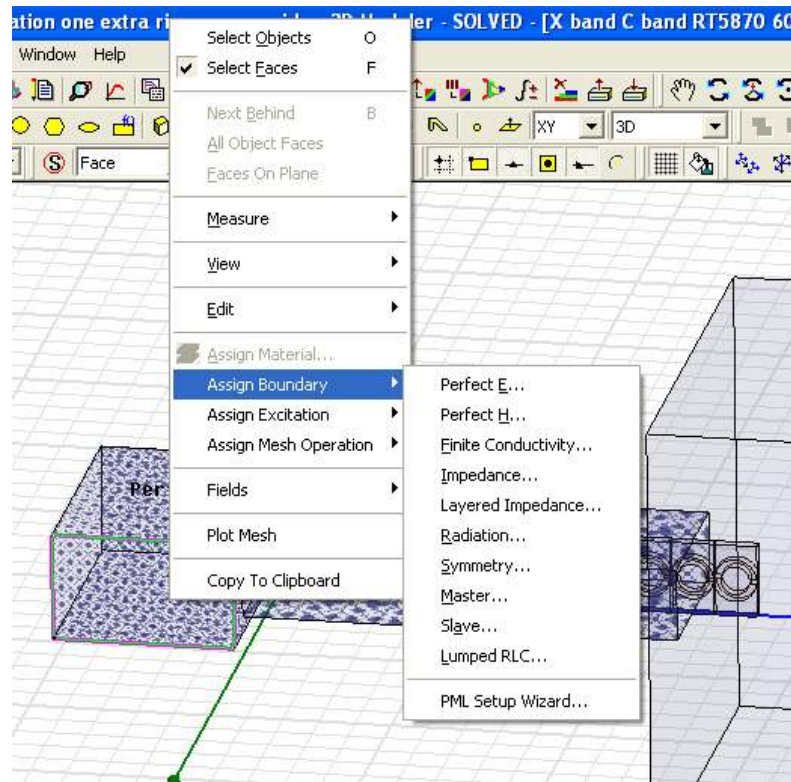


Figure 4.14: Boundary Assignment.

All the sides of the air box are selected to assign radiation boundary in a similar way. All assigned boundaries and excitations can be seen in the project manager window (figure 4.15). Selecting the particular boundary or an excitation will highlight the selection in the 3D model. Consistency of the assignment can be checked by doing this.

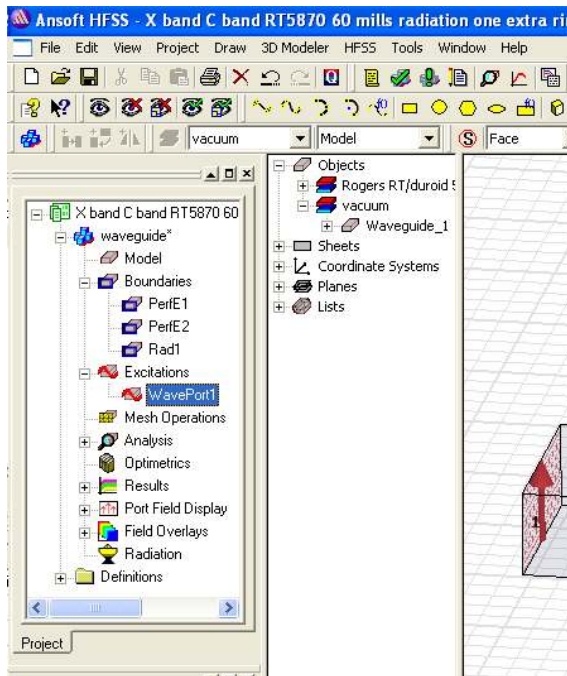


Figure 4.15: Boundary and excitations in project manager window.

At this stage the project is ready for analysis.

4.5.4 Solution setup and frequency sweep

Solution setup is defined under design in project manager to specify how HFSS will compute the solution. The solution setup is added by right clicking on the analysis in the design tree. In solution setup, solution frequency is specified as 10 GHz to instruct HFSS to perform adaptive analysis. Maximum number of passes is set to 11. Convergence error tolerance is set to 0.01 (figure 4.16). A number of solution setups can be added under Analysis tree.

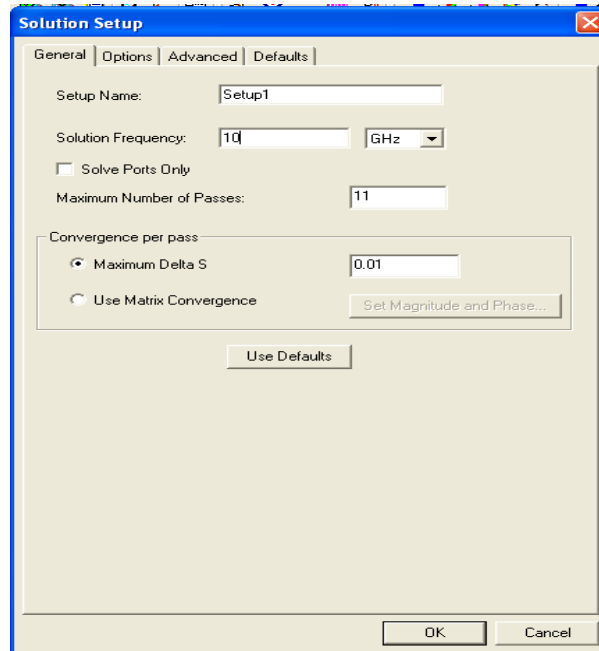


Figure 4.16: Solution Setup.

A smooth frequency response is expected for this design, so you will select a discrete sweep with a sufficient number of points. A discrete sweep estimates a solution for an entire frequency range at each frequency point. HFSS chooses the frequency points at which to solve the field solution so that the entire solution lies within a specified error tolerance. The sweep is complete when the solution meets the error tolerance criterion or generates the maximum number of solutions. The sweep is solved after the adaptive analysis is complete. The cutoff frequency of feeding waveguide is 4.3 GHz, and the cutoff frequency of X – band waveguide is 6.6 GHz. We need to simulate the project within this range to verify the left-handed transmission below the X – band cutoff frequency. The project is simulated from 4.3 GHz to 10 GHz (figure 4.17).

Before running the analysis, it is helpful to verify that all the necessary setup steps have been completed. This can be done by clicking Validation Check from the HFSS Tools menu (figure 4.18). After Validation, the project is ready to be analyzed. This can be done by right clicking on the Analysis in the design tree or by clicking on the

‘Analyze All’ button in the HFSS tools menu. HFSS computes the 3D field solution for every solution setup in the project. In this problem, Setup1 is the only setup.

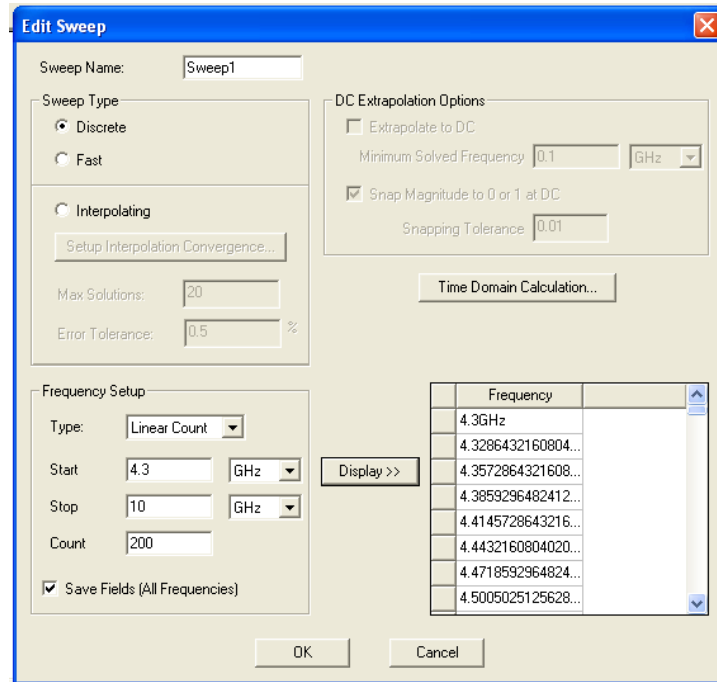


Figure 4.17: Frequency Sweep.

The solution process is expected to take some time depending on the complexity and error convergence value. When the solution is complete, a confirmation message appears in the Message Manager.

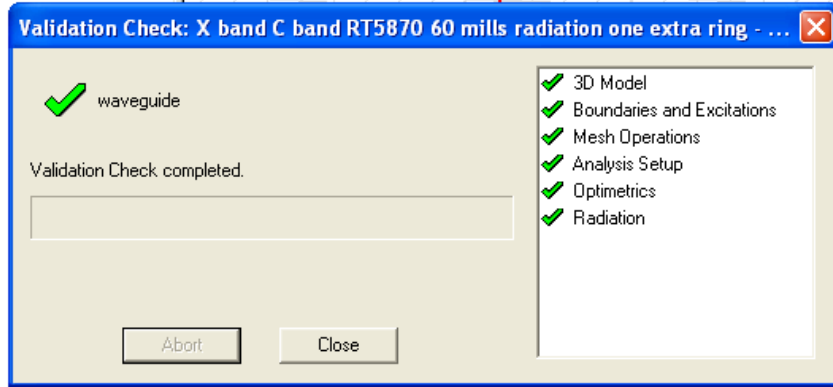


Figure 4.18: Validation Check.

4.6 Solution and post processing

When the simulation is complete, the results can be viewed by right clicking on Results in the Design tree, and selecting a specific report for the selected variable (figure 4.19). Different types of visual solutions can be plotted for the selected data. The data can also be exported in desired form.

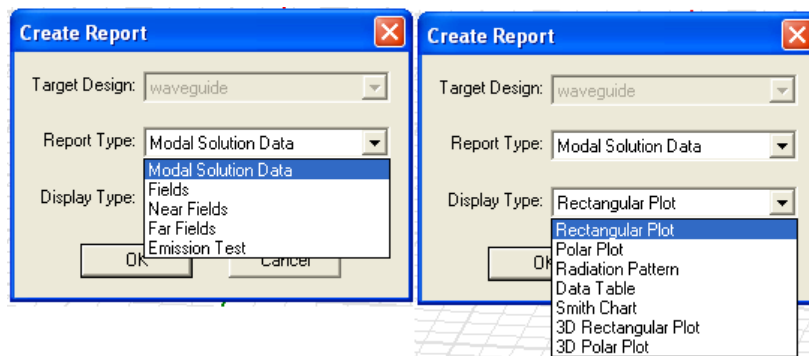


Figure 4.19: Plot selection.

Reflection coefficient S_{11} (negative of return loss) at the input port for the antenna is plotted in figure 4.20. From the plot, one can notice that the propagation passband is located well below the cutoff frequency of the X-band waveguide with the bandwidth of 500 MHz. Maximum return loss computed is 23 dB. Comparing this to previous work of miniaturization of waveguides in [7], [8], also presented in chapter 3, a better bandwidth and matching is obtained here.

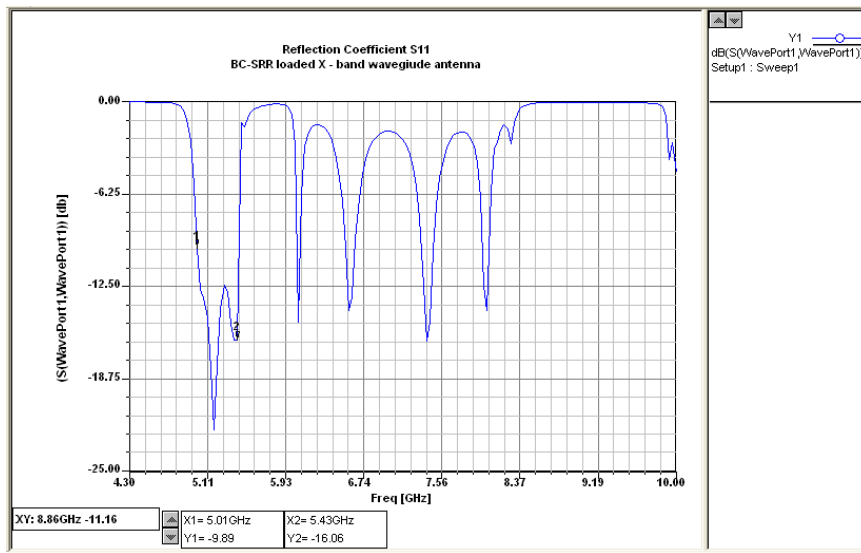


Figure 4.20: Return loss for the BC-SRR loaded waveguide antenna.

Existence of the passband below the cutoff frequency of the waveguide alone is not proof of a backward wave. In figure 4.21, which shows the phase and magnitude of the guided wave, it is clearly seen that in the passband, the phase of the wave increases unlike as in an ordinary waveguides where phase decreases. Thus, physically longer waveguides exhibit larger phase of S_{11} . This is because the direction of the phase velocity is opposite to the energy flow. This proves that there is a phase advance in such waveguides unlike phase delay in an ordinary waveguide. With this, one can conclude,

physically longer backward wave waveguide appears electrically shorter with phase advance.

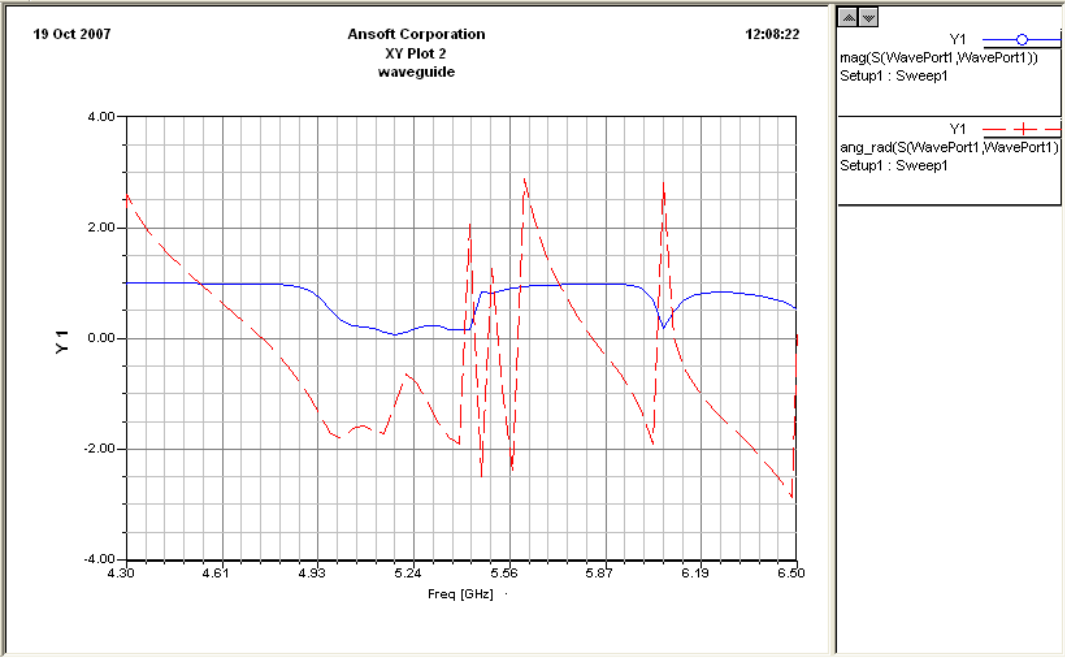


Figure 4.21: Phase (dotted) and magnitude (solid) of S_{11} for BC-SRR loaded waveguide antenna.

Figure 4.22 and figure 4.23 represent E-plane and H-plane radiation patterns at 5.15 GHz.

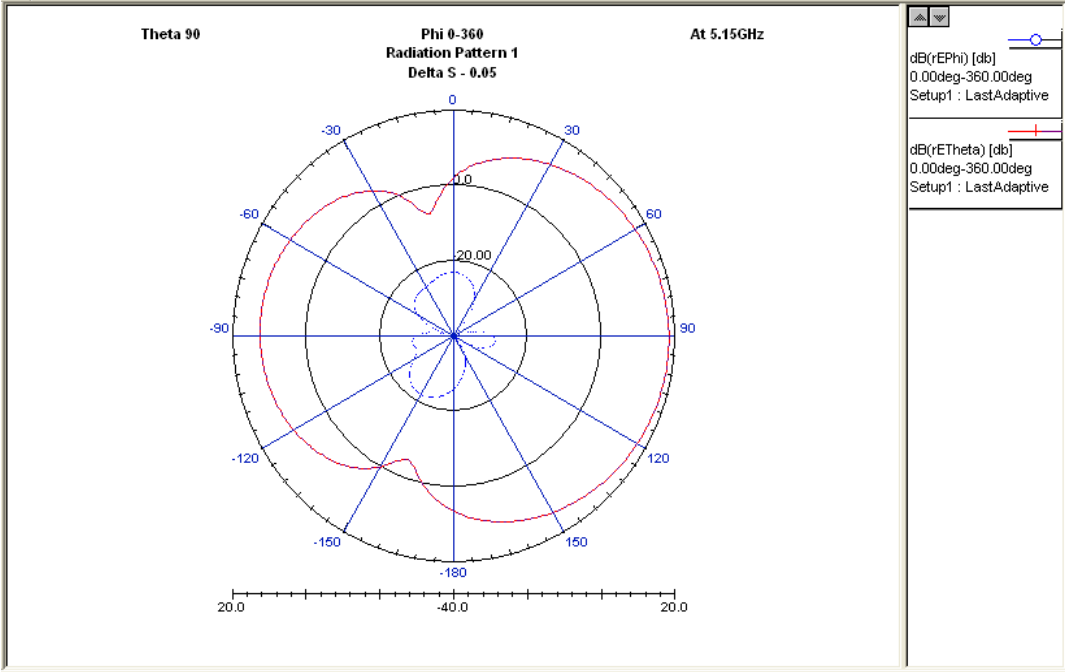


Figure 4.22: E-plane radiation pattern for BC-SRR loaded waveguide antenna (solid – co-polarized, dotted – cross-polarized).

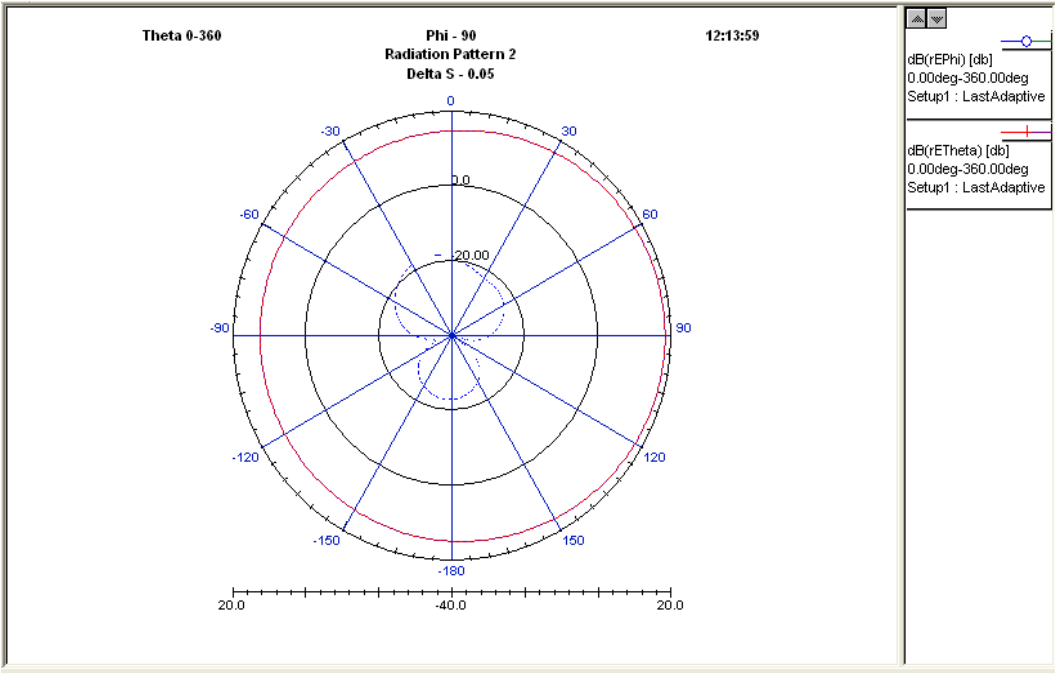


Figure 4.23: H-plane radiation pattern for BC-SRR loaded waveguide antenna (solid – co-polarized, dotted – cross-polarized).

4.7 Conclusion

Simulation of BC-SRR loaded X-band waveguide antenna radiating below the cutoff frequency was successfully carried out. According to simulations, the antenna operated at 5 GHz, 1 GHz below the cutoff frequency of the waveguide. The antenna had a bandwidth of 500 MHz. In chapter 5, experimental verification of the optimized BC-SRR loaded waveguide antenna is reported.

CHAPTER 5

LABORATORY MEASUREMENTS

5.1 Introduction

In this chapter we present experimental measurements of a fabricated prototype of the broadside coupled split - ring resonators (BC-SRR) loaded X-band waveguide antenna. Simulation results presented in the previous chapter are experimentally verified. For S-parameter measurements an HP 8719A network analyzer was used. Radiation pattern measurements were obtained using a far-field measurement setup with the same network analyzer. The antenna was placed in a chamber lined with high-performance pyramidal microwave absorbers for measurements. The reader is referred to appendix A for a detailed list of the experimental equipment used.

5.2 Fabrication

The rings for inclusion in the waveguide were fabricated using commercial 60 mil thick Rogers RT Duroid 5870 of relative permittivity 2.33. The HFSS simulation model was exported to AutoCAD in .dxf format and loaded to a QC5000 automated milling machine. Twelve split - rings were milled on both sides of a 10.16 mm strip of RT Duroid to fabricate the BC-SRR uniaxial negative permeability metamaterial. The fabricated structure is as shown in the figure 5.1.

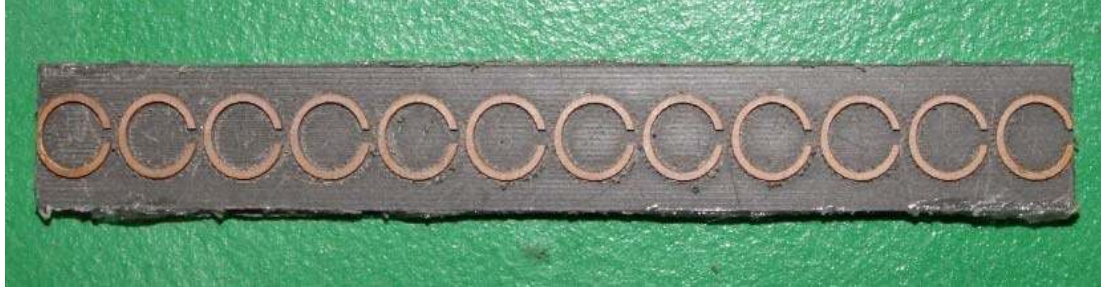


Figure 5.1: Photograph of array of twelve BC-SRR.

Dimension of the fabricated rings are shown in figure 5.2. The rings have outer radius of 3 mm and inner radius of 2 mm. Slit width was set to 0.5 mm. The lattice constant of unit cell was set to 6 mm.

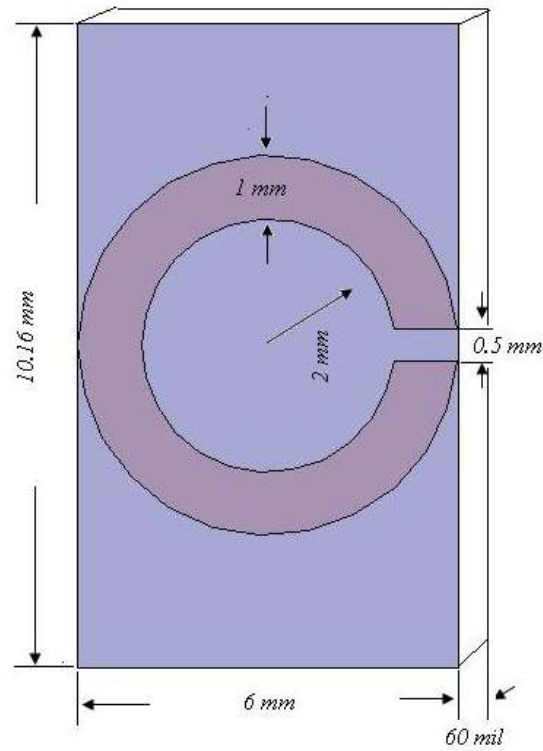


Figure 5.2: Unit cell dimensions.

5.3 Experimental setup and measurements

An array of twelve BC-SRR was placed in the symmetry plane of a 60 mm long X-band waveguide. The spacing between the rings was set to 6 mm. To ensure excitation of the first SRR in the array and to improve matching, the first ring was partially placed out from the X-band waveguide into the C-band waveguide and to improve radiation, the last ring was partially placed out from the open end of the waveguide with an extra ring. X-band waveguide loaded with SRR is excited by a C-band waveguide to coaxial adapter. C-band waveguide is fed by a coaxial line from the HP 8719A network analyzer.

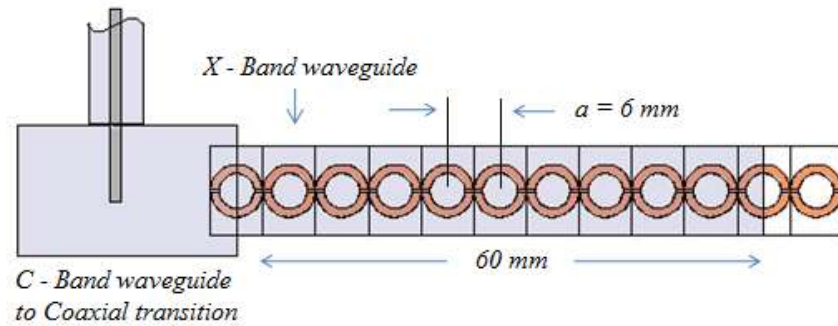


Figure 5.3: Schematic diagram of the prototype antenna.

A diagram of the prototype antenna is as shown in figure 5.3. No tuning stubs were used to match the C-band and X-band waveguides. Figure 5.4 shows a photograph of the antenna.

The antenna was tested using the HP 8719A network analyzer from 5 GHz to 7.5 GHz to verify the backward wave phenomenon and radiation below cutoff of the X-band waveguide predicted by the simulations.

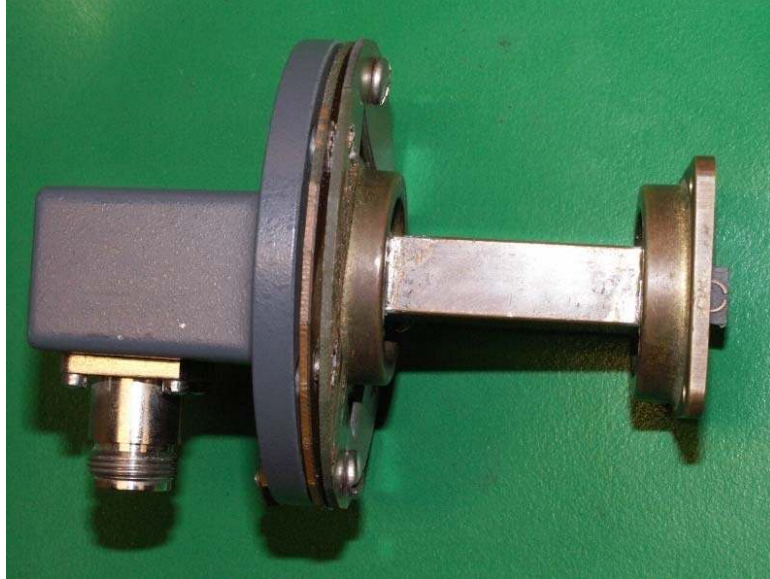


Figure 5.4: Photograph of the prototype antenna.

The measured reflection coefficient S_{11} of the antenna is shown in figure 5.5.

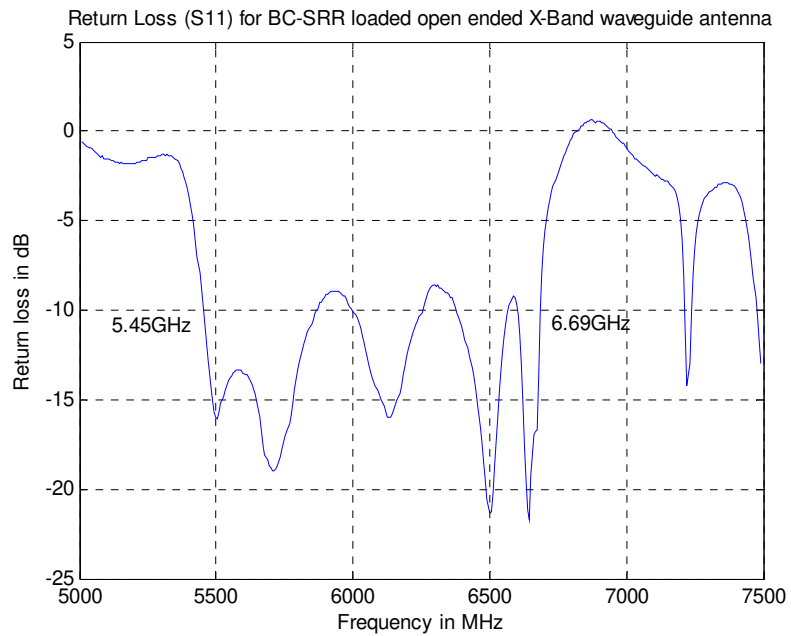


Figure 5.5: Measured S_{11} of the antenna.

One can clearly notice from the figure that the antenna starts radiating from 5.3 GHz which is over 1.0 GHz below the cutoff frequency of the X-band waveguide. From the -10 dB points, the antenna has a bandwidth of 1.24 GHz. Screen shot of the network analyzer is shown in figure 5.6.

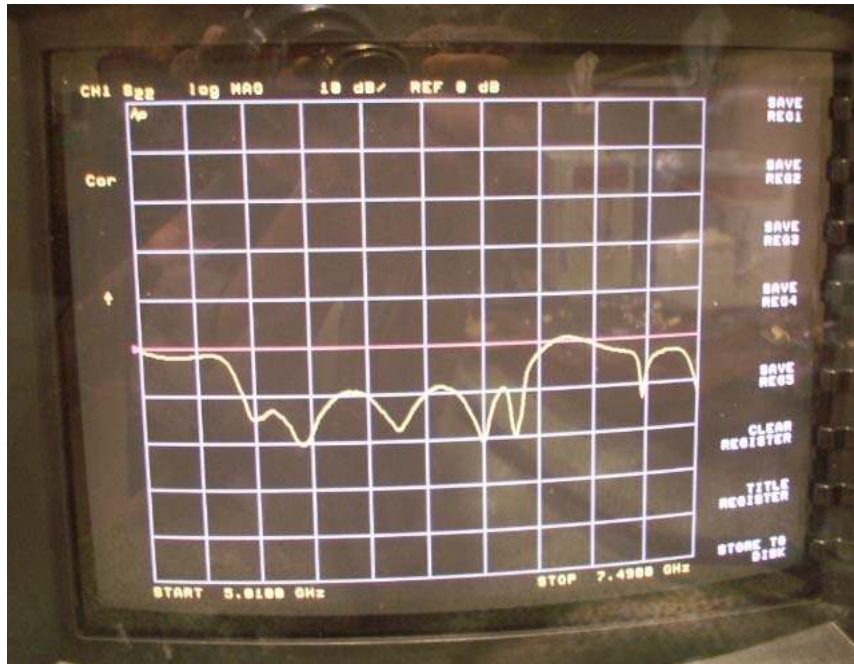


Figure 5.6: Screen shot of network analyzer.

In figure 5.7 it is clearly seen that whenever there is a passband, the phase of the signal increases giving rise to phase advance, unlike ordinary waveguides where phase decreases along the line at a frequency. This is because of direction of the phase velocity is opposite to the energy flow. With this, one can conclude, a physically longer backward wave transmission line appears electrically shorter with phase advance.

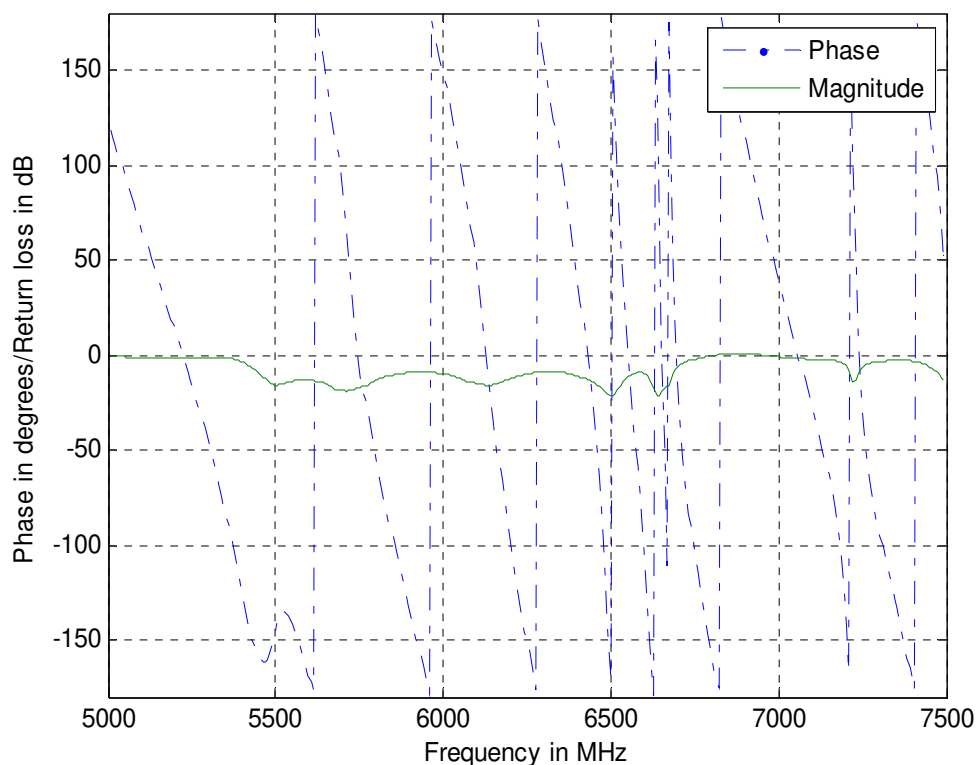


Figure 5.7: Measured phase and magnitude of input reflection coefficient (S_{11}).

Figure 5.8 shows comparison of simulated and measured reflection coefficients. Considering the crude fabrication techniques used, the measured result of the antenna is in good agreement with the simulated result. The shift in the passband between measured and simulated results seen in figure can be attributed to the fabrication irregularities and manual error in placing the 60 mil thick array of rings right at the symmetry plane of the waveguide. It can also be noticed that bandwidth of the measured result is greater than the simulated result.

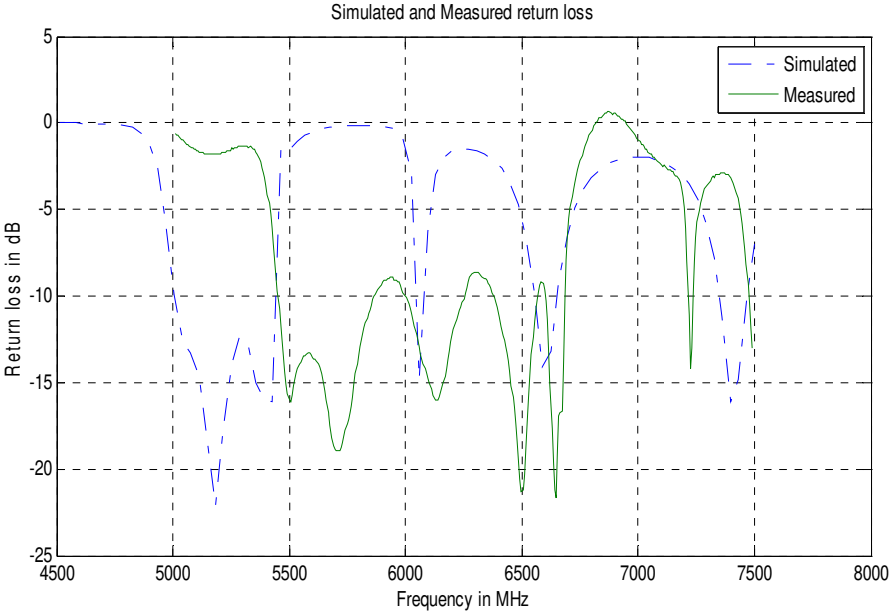


Figure 5.8: Measured and simulated reflection coefficient of the antenna.

The experimental setup for the radiation pattern measurement is shown in figure 5.9. A standard C-band coaxial-to-waveguide adapter was used as a receiving antenna at a distance of 1 m. The radiation pattern was measured with the help of the HP 8719A network analyzer.

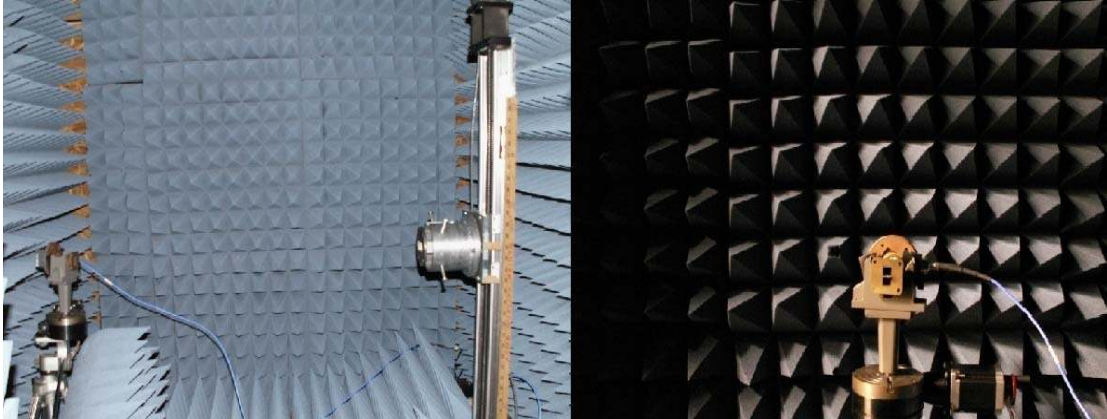


Figure 5.9: Experimental setup for measurement of radiation pattern.

Radiation patterns were measured at the lowest frequency in the passband, 5.5 GHz. Figure 5.10 and figure 5.11 shows the measured E-plane and H-plane radiation patterns, respectively, along with cross polarization.

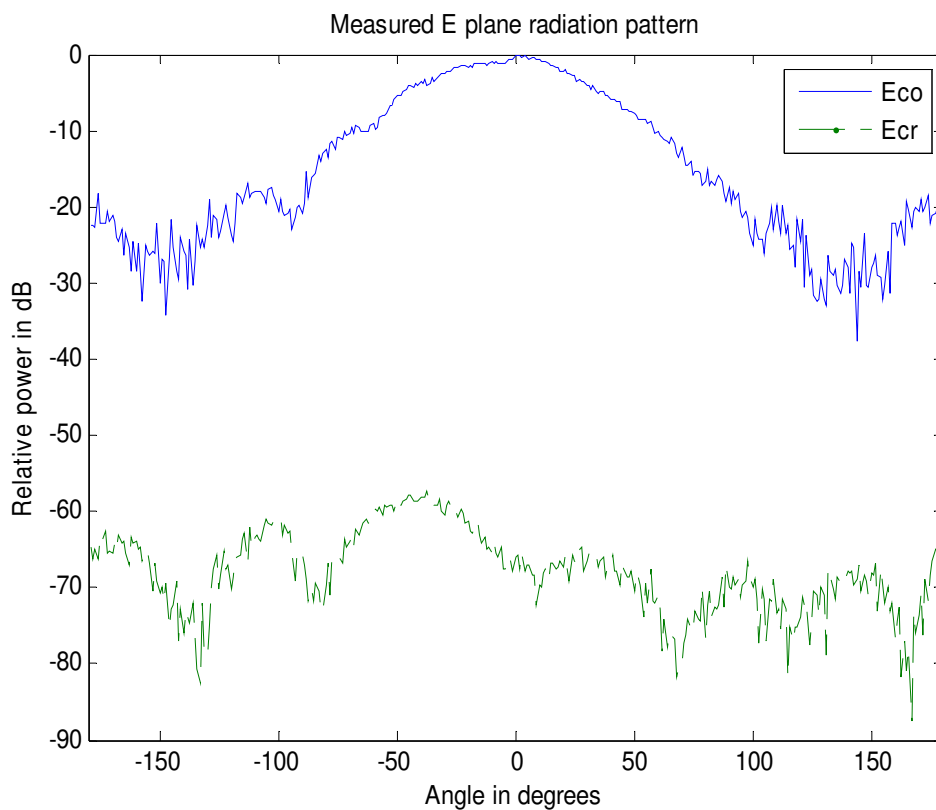


Figure 5.10: Measured E-plane co- and cross-polarized radiation patterns.

We can notice from the figure that the cross-polarization is lower than the co-polarization by 60 dB at the peak in the E-plane and 18 dB at the peak in the H-plane. Also, the antenna has very low directivity.

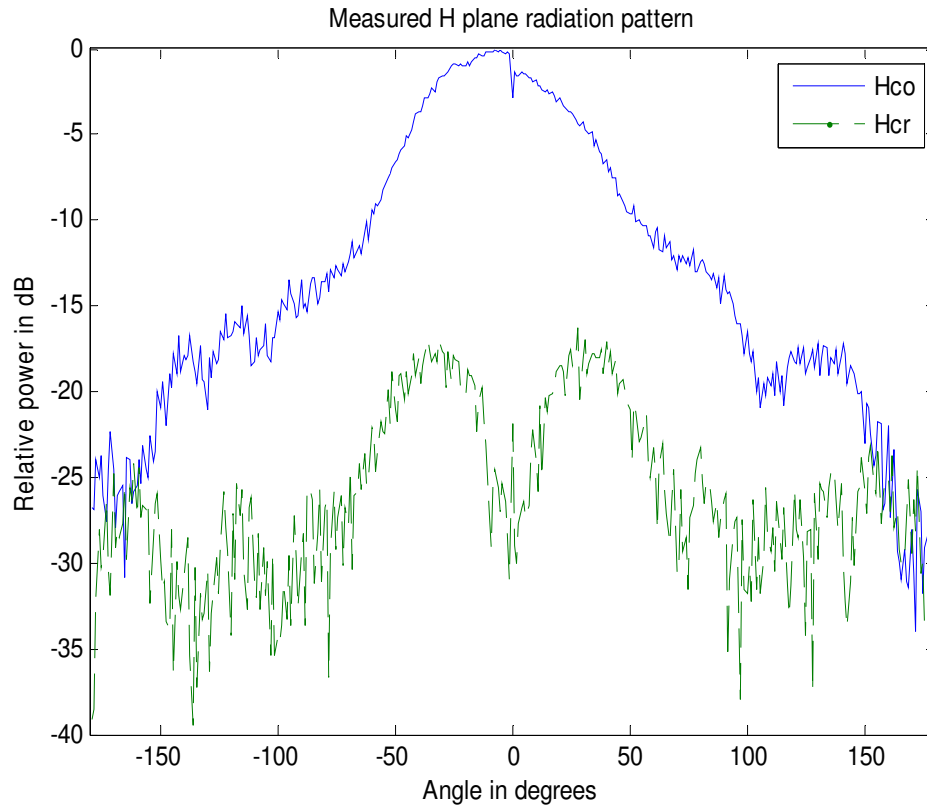


Figure 5.11: Measured H-plane radiation patterns.

Figure 5.12 compares the measured E-plane radiation pattern with the computed E-plane pattern. We can notice from the graph that the measured E-plane pattern is in good agreement with the HFSS simulation results.

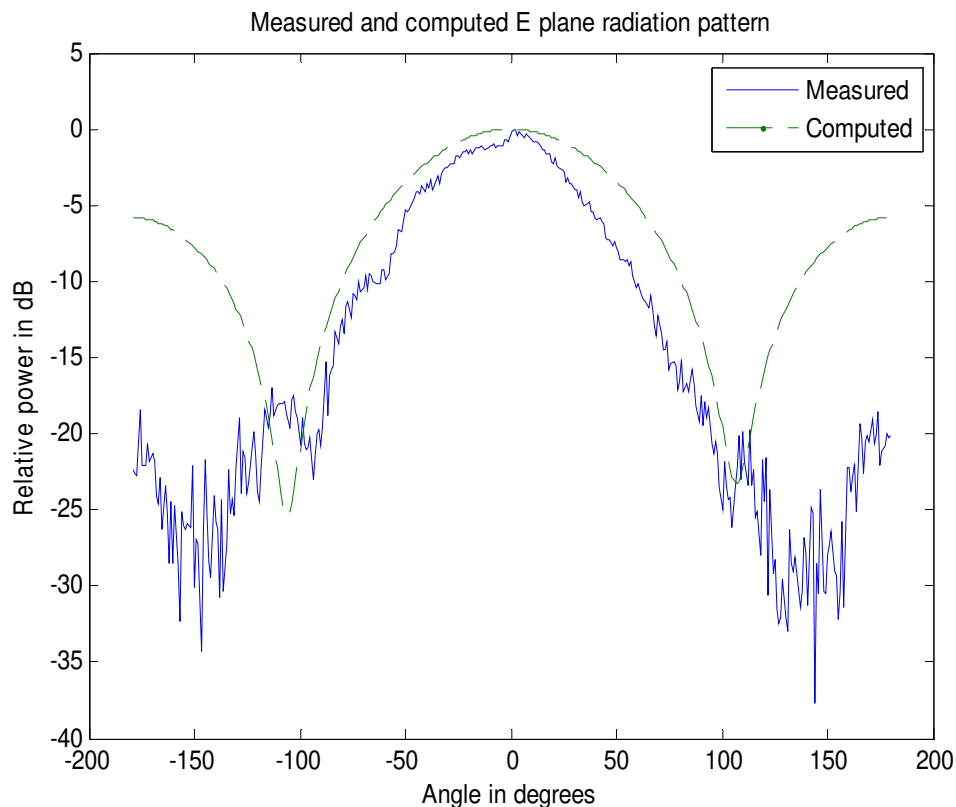


Figure 5.12: Comparison of measured and computed E plane radiation pattern.

Analyzing the experimental results and the HFSS simulation results, we come to the conclusion that there is a reasonable agreement. Inclusion of uniaxial negative permeability metamaterial in the symmetry plane of a simple open-ended antenna supports the radiation below cutoff frequency of the waveguide in the form of backward waves. To conclude, a miniaturized waveguide antenna based on metamaterial inclusion has been successfully designed, built, and tested.

Future research and improvement suggestions are noted below in chapter 6 of this work.

CHAPTER 6

CONCLUSIONS AND FUTURE DIRECTIONS

6.1 Highlights

This thesis has investigated design development, simulation, construction and testing of a miniaturized open-ended waveguide antenna. A novel technique was employed to miniaturize the open-ended radiator using electromagnetic metamaterials. The antenna is capable of radiating below the cutoff frequency of the waveguide by supporting backward waves.

After investigating various geometries of Uniaxial mu-negative (MNG) with different waveguides in simulation, broadside coupled split - ring resonators (BC-SRR) were selected as optimized metamaterial filling for miniaturization.

Ansoft HFSSTM 10 was used as the numerical analysis package for theoretical analysis of the proposed miniaturized waveguide. A brief introduction to HFSS as an effective tool for high-frequency structure analysis is given, and a comprehensive description of each step taken in creating the simulation of the antenna and mu-negative (MNG) structures were presented with post processing methods.

Based on the HFSS numerical simulation results, the miniaturized antenna was fabricated and tested. The experimental results were found to be in good agreement with the simulation results. The fabricated X-band antenna was capable of radiating below the cutoff frequency of the waveguide, at 5.3 GHz. Maximum measured return loss was 23 dB with 1.25 GHz of bandwidth. The measured radiation pattern agreed with that obtained from simulations.

6.2 Future work

The primary goal of the research was to miniaturize a waveguide antenna using novel electromagnetic metamaterial rather than classical dielectric inclusion. As described in chapter 3, the radiation property of the antenna does not depend on the cross section of the waveguide, but on the inclusion. Transverse width of such a waveguide can be, in principle, arbitrarily small. The lowest frequency of radiation, and therefore the miniaturization, is dictated by feasibility of fabrication of the metamaterial at the frequency of interest. In future work based on this method, a smaller, compact, square cross section waveguide could be designed. In this work only a few geometries of mu-negative (MNG) media are analyzed (EC-SRR, BC-SRR, square split - ring resonators, single ring resonators). An effort could be made to investigate other available geometrical configurations on different dielectric-constant substrates. The bandwidth of the backward wave propagation is governed by the dispersion property of the material filling. Future research could be directed towards characterization of metamaterials with better dispersion properties to develop a broadband antenna. New non - resonant type metamaterials reported in [38], [39], [40] could also be used to achieve greater bandwidth.

In this work, the X-band waveguide antenna was excited from C-band waveguide, no tuning stubs or any kind of matching was used to match the abrupt change in waveguide cross sections. Return loss could be improved with matching arrangements.

While measuring the radiation pattern, cables introduced attenuation. Better, low-loss cables and connectors could be used for a precise result.

Finally, numerical analysis and simulation of the structures is a very important step in development of an electromagnetic metamaterial medium. Simulation takes a lot of time and computer resources. HFSS 10, a full wave FEM electromagnetic solver, was used to simulate the structure in this work on a Pentium IV dual core processor with 2 GB of available memory. The simulation ran typically two days before it converged to desired

error tolerance. Finer meshing and more accurate results could be obtained from a better computing resource. Ansoft Corporation has recently released an advanced version, HFSS 11, which is faster and provides efficient solutions to larger wavelength structures. This newer version can be used for future work to reduce the amount of time required for simulations. Also, FDTD which is another popular method in the research community can be used for simulation.

REFERENCES

- [1] Waveguide handbook, Nathan Marcuvitz, 1986, IET.
- [2] YOSHIHIRO KONISHI, “Novel Dielectric Waveguide Components-Microwave Applications of New Ceramic Materials”, PROCEEDINGS OF THE IEEE, VOL. 79, NO. 6, JUNE 1991.
- [3] Cheng-Liang Huang, Donald P. Butler, “DIELECTRIC WAVEGUIDE RESONATOR WITH A SUPERCONDUCTIVE BOUNDARY LAYER”, PROCEEDINGS OF THE IEEE, VOL. 79, NO. 6, JUNE 1991.
- [4] A.P. Yevdokimov, V.V. Krizhanovsky, “OPTIMIZATION OF A HORN-PARABOLIC EXCITATION UNIT OF A PLANAR DIELECTRIC WAVEGUIDE”, MSMW 2001 Symposium Proceedings. Kharkov, Ukraine, June 4 -9, 2001.
- [5] Chi-Yang Chang, Wei-Chen Hsu, “Novel Planar, Square-Shaped, Dielectric-Waveguide, Single-, and Dual-Mode Filters”, IEEE TRANSACTIONS ON MICROWAVE THEORY AND TECHNIQUES, VOL. 50, NO. 11, NOVEMBER 2002.
- [6] Y. Fei-Ran, M. Kuang-Ping, Q. Yongxi, and T. A. Itoh, “Novel TEM waveguide using uniplanar compact photonic-bandgap (UC-PBG) structure,” IEEE Trans. Microw. Theory Tech., vol. 47, no. 11, pp. 2092–2098, Nov. 1999.
- [7] R. Marques, J. Martel, F. Mesa, and F. Medina, “Left-handed-media simulation and transmission of EM waves in subwavelength split-ring-resonator-loaded metallic waveguides,” Phys. Rev. Lett., pp. 183 901–183 904, Oct. 2002.
- [8] Silvia Harbar, Juraj Bartolic, Zvonimir Sipus, “Waveguide Miniaturization Using Uniaxial Negative Permeability Metamaterial”, IEEE TRANSACTIONS ON ANTENNAS AND PROPAGATION, VOL. 53, NO. 1, JANUARY 2005.

- [9] R. A. Shelby, D. R. Smith, S. C. Nemat-Nasser, and S. Schultz, “Microwave transmission through a two-dimensional, isotropic, left-handed metamaterial,” *App. Phys. Lett.*, vol. 78, no. 4, Jan. 2001.
- [10] *Electromagnetic Metamaterials: Towards Higher Frequencies*, David R. Smith.
- [11] J. B. Pendry, A. J. Holden, W. J. Stewart, and I. Youngs. “Extremely low frequency plasmons in metallic mesostructure,” *Phys. Rev. Lett.*, vol. 76, no. 25, pp. 4773–4776, June 1996.
- [12] J. B. Pendry, A. J. Holden, D. J. Robbins, and W. J. Stewart. “Low frequency plasmons in thin-wire structures,” *J. Phys. Condens. Matter*, vol. 10, pp. 4785–4809, 1998.
- [13] J. B. Pendry, A. J. Holden, D. J. Robbins, and W. J. Stewart, “Magnetism from conductors and enhanced nonlinear phenomena,” *IEEE Trans. Microwave Theory Tech.*, vol. 47, p. 2075, 1999.
- [14] L. Brillouin. *Wave Propagation in Periodic Structures*, McGraw-Hill, 1946.
- [15] J. R. Pierce. *Traveling-Wave Tubes*, D. Van Nostrand, 1950.
- [16] C. Caloz and T. Itoh. “Application of the transmission line theory of left-handed (LH) materials to the realization of a microstrip LH transmission line,” in *Proc. IEEE-AP-S USNC/URSI National Radio Science Meeting*, vol. 2, San Antonio, TX, pp. 412–415, June 2002.
- [17] C. Caloz, H. Okabe, T. Iwai, and T. Itoh. “Anisotropic PBG surface and its transmission line model,” in *URSI Digest, IEEE-AP-S USNC/URSI National Radio Science Meeting*, San Antonio, TX, pp. 224, June 2002.
- [18] A. Grbic and G. V. Eleftheriades. “A backward-wave antenna based on negative refractive index L-C networks,” in *Proc. IEEE-AP-S USNC/URSI National Radio Science Meeting*, vol. 4, San Antonio, TX, pp. 340–343, June 2002.

- [19] A. K. Iyer and G. V. Eleftheriades. “Negative refractive index metamaterials supporting 2-D waves,” in IEEE-MTT Int’l Symp., vol. 2, Seattle, WA, pp. 412–415, June 2002.
- [20] C. Caloz and T. Itoh. “Novel microwave devices and structures based on the transmission line approach of meta-materials,” in IEEE-MTT Int’l Symp., vol. 1, Philadelphia, PA, pp. 195–198, June 2003.
- [21] IEEE microwave magazine September 2004.
- [22] Lord Rayleigh, “On the passage of electric waves through tubes.” *Philos. Mag.*, Vol. 43, Cambridge Univ. Press, 1903.
- [23] O. Heaviside, “*Electromagnetic Theory*” vol. 1 1893.
- [24] Pavel A. Belov, “Subwavelength metallic waveguides loaded by uniaxial resonant scatterers”, *Physical Review E* 72, 036618 (2005). © 2005 by the American Physical Society.
- [25] Silvio Hrabar, Gordan Jankovic, “Scanning Leaky-wave Antenna based on a Waveguide filled with Plasma-like ENG Metamaterial”, IEEE MELECON 2006, May 16-19, Benalmádena (Málaga), Spain.
- [26] G. Lubkowski, C. Damm, B. Bandlow, R. Schuhmann, M. Schußler, T. Weiland, “Waveguide Miniaturization using Spiral Resonators and Dipole Arrays”, Proceedings of the 36th European Microwave Conference.
- [27] Silvio Hrabar, Zoran Eres, Juraj Bartolic, “Capacitively Loaded Loop as Basic Element of Permeability Meta-material”.
- [28] G.V. Eleftheriades, M.A. Antoniades, A. Grbic, A. Iyer, R. Islam, “ELECTROMAGNETIC APPLICATIONS OF NEGATIVE-REFRACTIVE-INDEX TRANSMISSION-LINE METAMATERIALS”.

- [29] S. Hrabar and J. Bartolic, "Capacitively loaded loop as basic element of negative permeability meta material," in Proc. 2002 European Microwave, Milan, Italy, 2002, pp. 357–361.
- [30] D. R. Smith, W. J. Padilla, D. C. Vier, S. C. Nemat-Nasser, and S. Schultz, "A composite medium with simultaneously negative permeability and permittivity," *Phys. Rev. Lett.*, vol. 84, no. 18, pp. 4184–4187, May 2000.
- [31] R. Marques, F. Medina, and R. Rafii-El-Idrissi, "Role of anisotropy in negative permeability and left-handed metamaterials," *Phys. Rev. B*, vol. 65, pp. 1–6, 2002.
- [32] Nader Engheta, Richard W. Ziolkowski, "Metamaterials, Physics and Engineering Explorations", Wiley Interscience, 2006.
- [33] R. Marques, F. Medina, and R. Rafii-El-Idrissi, "Role of anisotropy in negative permeability and left-handed metamaterials," *Phys. Rev. B*, vol. 65, pp. 1–6, 2002.
- [34] S. O'Brien and J. B. Pendry, "Magnetic activity at infrared frequencies in structured metallic photonic crystals," *J. Phys. Condens. Matter*, vol. 14, pp. 6383-6394, 2002.
- [35] J. Hungfu, L. Ran, H. Chen et. al, "Experimental confirmation of negative refractive index of a metamaterial composed of omega like metallic patterns", *Appl. Phys. Lett.*, vol. 84, pp. 1537-1539, Mar. 2004.
- [36] C. R. Simovski and S. He, "Frequency range and explicit expression for negative permittivity and permeability for an isotropic medium formed by a lattice of perfectly conducting omega particles based on quasi-static Lorentz theory", *Phys. Lett. A*, vol. 311, pp. 254-263, 2003.
- [37] H. Cheng, L. Ran et. al, "Left Handed metamaterials composed of only S-shaped resonators", *Phys. Rev. E*, vol. 70, 057605, 2004.
- [38] R. Marques, F. Mesa, J. Martel, F. Medina: "Comparative Analysis of Edge- and Broadside coupled SRR's for meta material design - Theory and experiments", *IEEE Trans. on Ant. and Prop.*, Vol 51, No. 10, Oct 2003.

- [39] C. Caloz and T. Itoh, "Application of the transmission line theory of left-handed materials to the realization of a microstrip LH line," *Proc. IEEE MTT-S*, pp. 412–415, 2002.
- [40] G. Eleftheriades, A. K. Iyer, and P. C. Kremer, "Planar negative refractive index media using periodically L-C loaded transmission lines," *IEEE Trans. Microw. Theory Tech.*, vol. 50, no. 12, pp. 2702–2712, Dec. 2002.
- [41] C. Caloz, A. Sanada, and T. Itoh, "Microwave circuits based on negative refractive index material structures," in *Proc. EuMc 2003, Munich, 2003*, pp. 389–392.
- [42] S. Hrabar and J. Bartolic, "Backward-wave waveguide based on uniaxial anisotropic negative permeability meta-material," *Proc. ICECOM 2003, 2003*.
- [43] S. Hrabar and J. Bartolic, "Simplified analysis of split - ring resonator used in backward meta-material," in *Proc. 2002 International Conference on Mathematical Methods in Electromagnetic Theory, Kiyev, Ukraine, 2002*, pp. 560–562.
- [44] R. Marques, F. Medina, and R. Rafii-El-Idrissi, "Role of anisotropy in negative permeability and left-handed metamaterials," *Phys. Rev. B*, vol. 65, pp. 1–6, 2002.
- [45] CHRISTOPHE CALOZ, TATSUO ITOH, "ELECTROMAGNETIC METAMATERIALS: TRANSMISSION LINE THEORY AND MICROWAVE APPLICATIONS The Engineering Approach", John Wiley & Sons, Inc. 2006.
- [46] V. Veselago. "The electrodynamics of substances with simultaneously negative values of ϵ and μ ," *Soviet Physics Uspekhi*, vol. 10, no. 4, pp. 509–514, Jan., Feb. 1968.
- [47] I. V. Lindell, S. A. Tretyakov, K. I. Nikoskinen, and S. Ilvonen. "BW media –media with negative parameters, capable of supporting backward waves," *Micr. Opt. Technol. Lett.*, vol. 31, no. 2, pp. 129–133, Oct. 2001.
- [48] S. A. Tretyakov, S. I. Maslovski, I. S. Nefedov, M. K. Kärkkäinen. "Evanescent modes stored in cavity resonators with backward-wave slabs," *Microwave Opt. Technol. Lett.*, vol. 38, no. 2, pp. 153–157, May 2003.

[49] A. Al`u and N. Engheta. “Guided modes in a waveguide filled with a pair of singlenegative (SNG), double-negative (DNG) and/or double-positive (DPS) layers,” *IEEE Trans. Microwave Theory Tech.*, vol. 52, no. 1, pp. 192–210, Jan. 2004.

[50] R. W. Ziolkowski. “Pulsed and CW gaussian beam interactions with double negative metamaterial slabs,” *Optics Express*, vol. 11, no. 7, pp. 662–681, April 2003.

[51] Agilent Technologies USB/LAN/GPIB Interfaces, Connectivity Guide.

APPENDIX A

EQUIPMENT LIST

Following specialized equipment were used in this thesis.

- X – Band Waveguide (WR – 90).
- C – Band waveguide (WR – 137) to coaxial adapter.
- 60 mil thick Roger’s RT Duroid 5870 of relative permittivity 2.33.
- HP 8719A network analyzer.
- Far – field radiation measurement setup.
- Computer controlled positioning system.
- NI – GPIB interface card.
- Personnel Computer.
- QC5000 automated milling machine.
- SMA Cable.
- 50 Ω Air Cable.
- 85032B 50 Ω Type – N network analyzer calibration kit.
- Microwave Absorbers.
- Ansoft HFSS 10.
- AutoCAD.
- Max 420 Indexer.
- SIN – 10 Serial Adapter.
- AMH23-258-3 Stepper Motor.
- 3700 CNC Turn Table/Rotor

PERMISSION TO COPY

In presenting this thesis in partial fulfillment of the requirements for a master's degree at Texas Tech University or Texas Tech University Health Sciences Center, I agree that the Library and my major department shall make it freely available for research purposes. Permission to copy this thesis for scholarly purposes may be granted by the Director of the Library or my major professor. It is understood that any copying or publication of this thesis for financial gain shall not be allowed without my further written permission and that any user may be liable for copyright infringement.

Agree (Permission is granted.)

Student Signature

Date

Disagree (Permission is not granted.)

Vikram Hegde

November 30, 2007

Student Signature

Date